Seismic Image of the Central to Southern Andean Subduction Zone Through Finite-Frequency Tomography

Y. Kondo[1], M. Obayashi[1, 2], H. Sugioka[1], H. Shiobara[3], A. Ito[2], M. Shinohara[3], H. Iwamori[3], M. Kinoshita[3], M. Miller[4], C. Tassara[5], and J. Ojeda[6,7]

[1]Department of Planetology, Faculty of Science, Kobe University, 1-1, Rokkodai-cho, Nada-ku, Kobe, Hyogo, 657-8501, Japan

[2]Japan Agency of Marine-Earth Science and Technology, 2-15 Natsushima-cho, Yokosuka, Kanagawa, 237-0061, Japan

[3]Earthquake Research Institute, The University of Tokyo, 1-1-1, Yayoi, Bunkyo-ku, Tokyo, 113-0032, Japan

[4]Department of Geophysics, University of Concepción, Casilla, 160-C, Concepción, Chile

[5]Faculty of Science, Arturo Prat University, Arturo Prat, 2120, Iquique, Chile

[6]Departamento de Geofísica, Universidad de Chile, Av. Blanco Encalada, 2002, Santiago, Chile

[7]Université Paris Cité, Institut de Physique du Globe de Paris, CNRS, Paris, France

Corresponding author: Yuko Kondo (ykondo@stu.kobe-u.ac.jp)

Key Points:

- The results of a P-wave teleseismic tomography study of central to southern Andean subduction zones are presented.
- A fast-velocity anomaly beneath the Nazca slab was revealed and interpreted as a relic Nazca slab segment.
- A slow-velocity anomaly associated with the Patagonian slab window was observed, constraining the maximum depth the window affects.

Abstract

This study presents new seismic imaging of the Andean subduction zone through P-wave hybrid finite-frequency and ray-theoretical tomography. We measured both differential and absolute traveltimes using broadband seismic waveforms from stations in an array of ocean-bottom seismographs near the Chile Triple Junction (CTJ) and stations within 30° from the array. These data were combined with the global traveltime dataset to obtain a global P-wave velocity structure with a focus on central to southern South America. The new tomographic image showed the Nazca slab geometry as a continuous fast anomaly, which is consistent with seismic activity and prior slab models. Furthermore, two notable structures were observed: a broad extension of the fast anomaly beneath the Nazca slab at 26–35° S and a slow anomaly east of the CTJ. The checkerboard resolution and recovery tests confirmed the reliability of these large-scale features. The fast anomaly, isolated from the Nazca slab, was interpreted as a relic Nazca slab segment based on its strong amplitude and spatial coincidence with the current Pampean and past Payenia flat slab segments. The slow anomaly near the CTJ was consistent with the previously inferred extent of the Patagonian slab window. Moreover, the active adakitic volcanoes are aligned with the southern edge of the anomaly, and the plateau basalts are located within the anomaly. Our model showed that the slow anomaly extended to a depth of up to 250 km, suggesting a depth limit that the asthenospheric window can influence.

Plain Language Summary

The western margin of South America is one of the largest subduction zones on the Earth and has provided insights into the subduction dynamics of relatively young oceanic plates. We developed a new seismic P-wave velocity model beneath the Central to Southern South America using teleseismic traveltime tomography. Traveltime data picked from broadband seismograms and collected from the global catalog by the International Seismology Centre were used for the tomographic inversion. Our model shows mantle structure to the uppermost part of the lower mantle at a depth of ~1,000 km. The geometry of the Nazca slab in our model agrees well with other seismic imagings and slab models. Beneath the Nazca slab, a fast velocity anomaly was observed and interpreted as a relic Nazca slab segment. Moreover, strong, slow anomalies in the upper mantle were observed to be located on east side of where the actively spreading Chile Ridge is subducting. The extent of anomalies and comparison with volcanism suggest a depth limit that the asthenospheric window can influence of up to 250 km.

1 Introduction

The Chile Trench is a subduction zone more than ~7,000 km in length, where the Antarctic and Nazca plates are currently subducting eastward beneath the South America plate (Figure 1). The subduction system in Chile is characterized by a young, warm oceanic lithosphere that subducts less steeply, including horizontal flat-slab segments (e.g., Barazangi & Isacks, 1976; Cahill & Isacks, 1992; Suárez et al., 1983). The convergence rates along the trench are relatively constant at ~6.7 cm/yr at an azimuth of ~77º (DeMets et al., 2010). The age of the Nazca plate varies systematically along the Chile Trench, from 0 Myr at the Carnegie Ridge (~7° S) to 50 Myr at 20° S and 0 Myr at the Chile Ridge (Müller et al., 2008). At ~46° S, the Chile Ridge subducts against the Chile Trench to form the Chile Triple Junction (CTJ). This region is a unique example of the subduction of an actively spreading ridge.

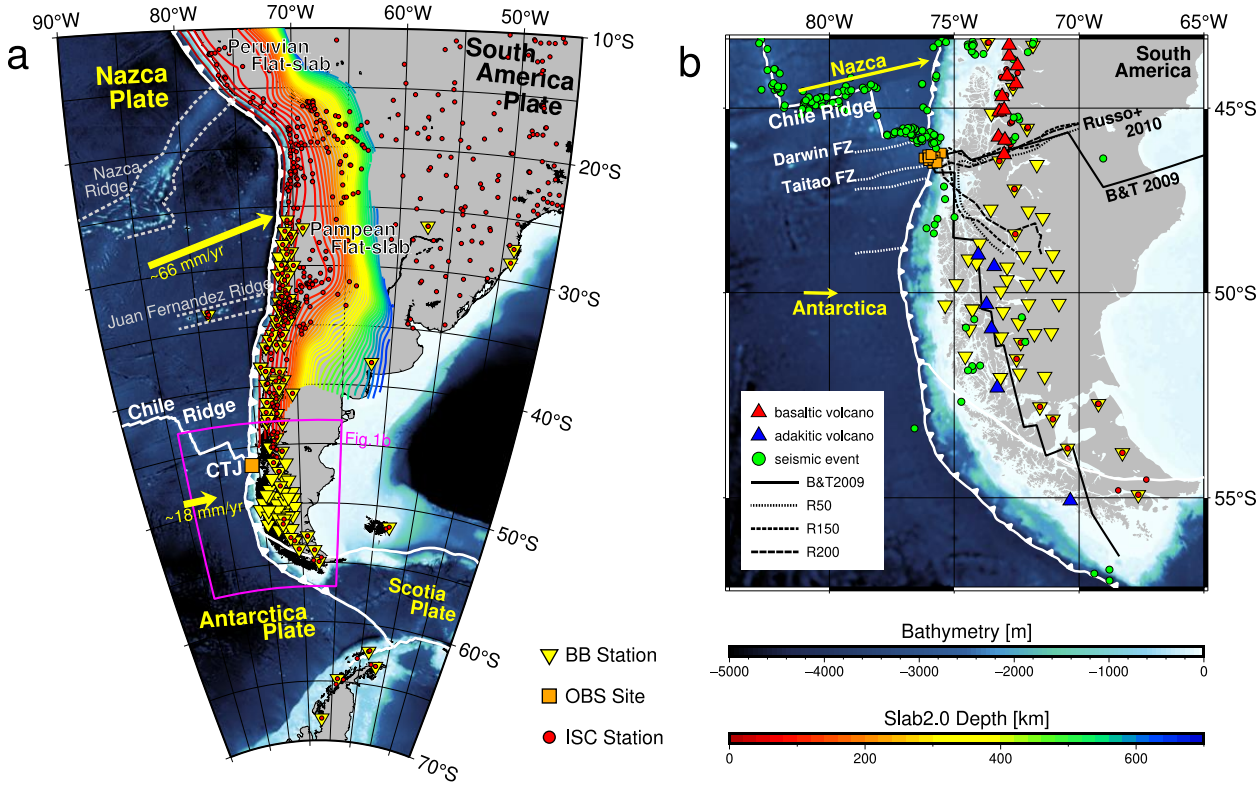

Figure 1. Tectonic settings of the central to southern Andean subduction zone. The yellow triangles represent the broadband seismic stations from IRIS, and the orange square indicates the location of 12 Ocean Bottom Seismometers, which were used to measure traveltimes. Red circles indicate stations in the International Seismology Centre's global traveltime data. Within the area of the anticipated Patagonian slab window, there are dense broadband stations that have not yet been included in ISC's global data. (**a**) Map of Central-Southern South America, showing Nazca slab contours of the Slab2 model as colored lines (Hayes et al., 2018), current plate boundaries as solid white lines (United States Geological Survey), and the primary aseismic ridges as dotted white lines. The yellow arrows indicate the motion of the Nazca and Antarctica plates relative to South America (DeMets et al., 2010). Slab2 model contours follow the depth color scale below. (**b**) Map of Southern Patagonia with the estimated extensions of the Patagonian slab window delineated by the black solid line (BT2009) as proposed by Breitsprecher & Thorkelson (2009). The black dotted lines, R50, R100, and R200, represent the iso-depths of the slab window edge according to the Vp anomaly contour by Russo et al. (2010). The red and blue triangles signify the basaltic and adakitic volcanism along the volcanic arc, respectively (Siebert & Simkin, 2002), while the green dots indicate the epicenters of the seismic event with magnitudes greater than 4, showing a seismic gap within the window.

1.1 Subduction of Nazca Plate

Seismic activity, volcanism, topography, and deformation along the western edge of South America exhibit significant variations along the trench strike. These variations are primarily attributed to complex geological processes associated with spatial and temporal changes in the geometry, dip angle, and behavior of the subducting Nazca plate (e.g., Chen et al., 2019; Dávila & Lithgow-Bertelloni, 2013; Espurt et al., 2008; Kay & Coira, 2009; Martinod et

al., 2013; Ramos, 1999; Ramos & Folguera, 2009). In particular, the flat subduction of the Nazca plate has been attributed to its influence on the overriding plate, causing the cessation of arc volcanism, the uplift and deformation of the Andes, crustal thickening, and basement uplift over a broad area (e.g., Cristallini & Ramos, 2000; Kay & Mpodozis, 2002; Ramos et al., 2002).

Understanding the character and behavior of the Nazca slab in comprehending the complexity and uniqueness of the subduction system of the Andean margin has prompted various seismic imaging studies in this region. Many regional teleseismic tomography studies have provided insights into the structure of the Nazca slab in the upper mantle, revealing features such as slab holes and tearing (Pesicek et al., 2012; Portner et al., 2017; Scire et al., 2016), lithospheric delamination (e.g., Bianchi et al., 2013), and variations in slab thickness (Scire et al., 2017). More recently, continental-scale teleseismic tomography studies covering the lower mantle have improved the resolution and provided key constraints on the detailed structure of the Nazca slab (Ciardelli et al., 2022; Mohammadzaheri et al., 2021; Portner et al., 2020; Rodríguez et al., 2020). The observed behavior of the slab in global models is generally consistent with these regional models (e.g., Lu et al., 2019; Obayashi et al., 2013; Simmons et al., 2012). Such models show similar trends; for example, transitions from normal to flat subduction along the strike and dip directions, with the slab directly plunging into the lower mantle in the northern region of ~20° S.

Flat subduction segments, which are unique features along the western margin of South America, have been extensively debated (e.g., Espurt et al., 2008; Gutscher et al., 2000; Manea et al., 2017; Marot et al., 2014; Ramos & Folguera, 2009). Three well-known flat slab segments exist: the Mexican (5°–8° N), Peruvian (5°–15° S), and Pampean flat slabs (26°–32° S). They lie horizontally for hundreds of kilometers before steeply subducting into the deep mantle, although their horizontal dimensions and flattening depths are different. The presence of flat-slab subduction has been reported based on seismicity (e.g., Barazangi & Isacks, 1976; Pesicek et al., 2012), volcanism (e.g., Kay & Mpodozis, 2002), electrical conductivity analysis (e.g., Burd et al., 2013), and seismic imaging studies. The seismic velocity structures of flat slabs and their surrounding regions down to ~150 km and those in the upper mantle have been resolved by surface wave tomography (e.g., Celli et al., 2020; Feng et al., 2007) and regional body wave tomography (e.g., Gao et al., 2021; Portner et al., 2017; Scire et al., 2016), respectively. The locations of the flat-slab segments coincide spatially with the intersections of the aseismic ridges and Chile Trench. Consequently, it has been widely argued that the current Peruvian and Pampean flat slabs are associated with the subduction of the Nazca and Juan Fernández ridges, which originated from hotspot volcanism (Figure 1a, e.g., Gutscher et al., 2000; Kay & Mpodozis, 2002). Recent numerical modeling studies have revealed that the overriding continental plate thickness, plate kinematics, and/or asthenospheric dynamics may play essential roles in the development of flat-slab subduction and oceanic plateau subduction (Manea et al., 2017; 2012, and references therein). However, the mechanisms and tectonics of flat-slab subduction remain controversial (e.g., Gao et al., 2021; Liu & Currie, 2019).

Slow anomalies just below the Peruvian and Pampean flat slabs have been identified (Celli et al., 2020), and their interactions with the slab have been discussed (Rodríguez et al., 2020). Several possible models have been proposed to explain these slow anomalies, including asthenospheric upwelling associated with locally thinned oceanic lithosphere related to the Nazca Ridge (Scire et al., 2016), the presence of volatile-rich subslab mantle flow, increased temperature and/or decompression melting due to small-scale vertical flow (Antonijevic et al.,

2016), and the entrainment of hotspot material (Portner et al., 2017). Moreover, a high-velocity anomaly disconnected from the subducting Nazca slab was reported beneath the slab. Teleseismic shear wave tomography by Rodríguez et al. (2020) and full waveform inversion by Gao et al. (2021) detected a fast S-wave velocity anomaly beneath the Chile Trench in the latitude range of 25–35° S. They interpreted this anomaly as either a remnant of a completely subducted slab or a detached Nazca slab. However, the geometry and amplitude of non-slab seismic anomalies, including slow and fast subslab anomalies, vary widely among models and remain debatable.

1.2 Patagonian Slab Window

The actively spreading Chile Ridge has been subducting since the mid-Miocene (Figure 1b, Breitsprecher and Thorkelson, 2009; Cande et al., 1987; Eagles et al., 2009), forming the CTJ and providing an important opportunity to study ridge subduction. Since the 1980s, numerous geological, geochemical, and geophysical studies have been conducted on the subduction of the Chile Ridge (e.g., Bangs & Cande, 1997; Gallego et al., 2010; Kaeding et al., 1990; Maksymowicz et al., 2012). These studies revealed that the subduction of the Chile Ridge segments has widespread effects on the overriding continent plate: the pronounced gap in the Patagonian volcanic arc and seismicity along the subduction zone (Agurto-Detzel et al., 2014; Cande & Leslie, 1986; DeLong et al., 1979; Gutiérrez et al., 2005; Ramos & Kay, 1992), adakitic volcanism near the slab edges (Bourgois et al., 2016; Stern & Kilian, 1996; Thorkelson & Breitsprecher, 2005), back-arc–like plateau basalts in Patagonia (Espinoza et al., 2005; Gorring et al., 1997; Ramos & Kay, 1992), geologically recent volcanic activity anomalously close to the trench (Forsythe et al., 1986; Lagabrielle et al., 1994; 2000), anomalous isotopic compositions of the lavas from the southern Chile Ridge (Karsten et al., 1996), obduction of the Plio-Pleistocene Taitao ophiolite (Bourgois et al., 1996; Lagabrielle et al., 2000; Nelson et al., 1993; Veloso et al., 2005), anomalously large negative bouguer gravity anomaly and extremely high heat flow on the eastern side of the CTJ (Ávila & Dávila, 2018; Cande et al., 1987; Murdie et al., 2000), and positive dynamic topography (Boutonnet et al., 2010; Guillaume et al., 2009; 2010; Mark et al., 2022).

When a spreading ridge intersects a trench, the ridge-transform system is surrounded by a hot asthenospheric mantle as it descends. The ridge-transform system continues to spread, and no new lithosphere is formed along the subducted ridge. Consequently, the slab window, the gap between the edges of the subducted-ridge transform system, progressively expands (DeLong et al., 1979; Dickinson & Snyder, 1979; Groome & Thorkelson, 2009; Thorkelson, 1996; Thorkelson & Breitsprecher, 2005; Thorkelson & Taylor, 1989). Slab windows provide gaps through which the asthenospheric mantle can flow and mix, resulting in local thermal anomalies in the asthenosphere and strong chemical and physical effects on the surrounding mantle (Thorkelson, 1996; Thorkelson & Taylor, 1989).

The formation of the Patagonian slab window commenced at approximately 18 Ma when the Chile Ridge began to subduct at approximately 54° S on the South American continent (Breitsprecher & Thorkelson, 2009). Since then, the window has gradually extended as the triple junction has migrated northward by approximately 1,000 km, with major ridge segments subducting at 14, 10, 6, 3, and 100 ka to the present (Bourgois et al., 2000; Breitsprecher & Thorkelson, 2009). The extent of the Patagonian slab window has been estimated using kinematic reconstruction (Breitsprecher & Thorkelson, 2009) and imaged using seismic

tomography as upper mantle low-seismic-velocity anomalies (Gallego et al., 2010; Mark et al., 2022; Miller et al., 2023; Russo et al., 2010).

Russo et al. (2010) first delineated the Patagonian slab window to a depth of 200 km using regional body-wave tomography with teleseismic data recorded on temporal seismic networks. Recently, Miller et al. (2023) enhanced the tomographic image of the Chile Ridge subduction using a technique similar to that employed by Russo et al. (2010) with a different dataset. Their results showed pronounced slow anomalies with an amplitude of ~3% between depths of 100 and 300 km on the east side of the CTJ, along with a fast anomaly interpreted as a young Nazca plate on its northern side. They discussed in detail the geometry of the subducted Nazca plate near the CTJ and proposed slab tears along the fracture zone among subducted Nazca plate segments. The results obtained from the kinematic reconstruction and seismic models are in good agreement. Previous body wave studies on slab windows focused on an area of hundreds of kilometers around the CTJ. Mark et al. (2022) provided an extensive image using Rayleigh wave tomography across the entire Patagonian slab window. They observed slow S-wave velocities within a slab window at shallow depths and discussed the thermal erosion of the lithosphere in the young slab window. To comprehensively discuss the mantle response to slab window formation, a more extensive and deep seismic velocity structure that provides constraints on the full extent and depth of the window is required. However, other regional and global tomography models, which cover broader areas, have limited resolution in southern South America owing to the paucity of stations and low seismic activity.

In this paper, we report a new three-dimensional P-wave velocity model beneath central to southern South America based on traveltime data measured using broadband seismograms collected in the target region and recent our seafloor observations near the CTJ. Our findings suggest two remarkable structures: fast anomalies beneath the Nazca slab and slow anomalies east to the CTJ. We then discuss the origin of the subslab fast anomalies and the extent of the Patagonian slab window based on these slow anomalies.

2 Data

An Ocean Bottom Seismograph (OBS) array was deployed directly above the CTJ for almost two years, from January 2019 to January 2021 (Ito et al., 2023). This OBS array comprised seven broadband OBSs and five long-term OBSs. We collected seismograms from ~100 onshore broadband stations within 30° of the OBS arrays for the same period as the OBS observations via the Incorporated Research Institutions for Seismology (IRIS) Data Management Center (Figure 1a). Most of these onshore broadband stations are located along the Chilean coast between 25° and 55° S. Only a few stations are located in the interior and eastern passive margins as well as along the coast of Antarctica. Using the data from the OBS array and onshore broadband stations, we measured two types of traveltimes for tomography inversion: absolute P-wave and finite-frequency differential P-wave traveltimes between every pair of stations.

Absolute P-wave traveltimes were obtained using the Adaptive Stacking method (Rawlinson & Kennett, 2004). In this method, P-wave waveforms were first stacked along the predicted traveltime curve using the seismic velocity model IASP91 (Kennett & Engdahl, 1991) to calculate a reference trace. Subsequently, the alignment of the individual traces and stacked reference trace was iteratively improved by time-shifting each trace to minimize the misfit from the reference trace, leading to an estimation of the residuals from the model prediction. The

absolute traveltimes for each station were obtained by adding the time shift of each station from the reference trace to the onset time picked on the high-signal-to-noise ratio reference trace.

Differential traveltimes were measured by cross-correlating band-passed seismograms for all possible station pairs. In this study, we measured the traveltimes for 10 frequency bands with center periods of 30, 21, 15, 10.6, 7.5, 5.3, 3.7, 2.7, 1.9, and 1.3 seconds. The differential traveltime is defined as the time shift between bandpassed waveforms at which the cross-correlation function achieves the maximum value of the cross-correlation coefficient (Dahlen et al., 2000). The appropriate time windows were set to be sufficiently longer than the center period of each frequency band and to include the manually picked first arrival time. Measurements with correlation coefficients of 0.9 or higher were selected and visually confirmed. We obtained a total of 1,642 P-wave absolute traveltimes for 32 events during the OBS observation period and 224,549 P-wave differential traveltimes for 25 events, as shown in Figure 2. Prior to the inversion, the traveltime residuals were corrected for topography and ellipticity.

In addition to these regional data, global onset times from January 1964 to March 2020 published by the International Seismology Centre (ISC) were obtained (Figure S1). We extracted events with a magnitude of ≥ 4.0 and several P observations > 50 and selected to be distributed as uniformly as possible in space and time. Traveltime data with residuals of 10 s or more were removed as outliers. Consequently, we obtained 31,011,580 traveltime data for approximately 123,000 events. The ISC catalog contains data from short-period seismometers and broadband networks that are not available in the IRIS data management center, resulting in more stations in the eastern region than in the regional array.

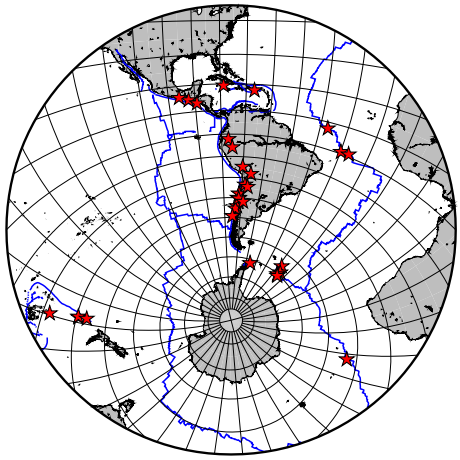

Figure 2. Distribution of the events (red stars) within a distance of 90º from the OBS array used to measure traveltimes.

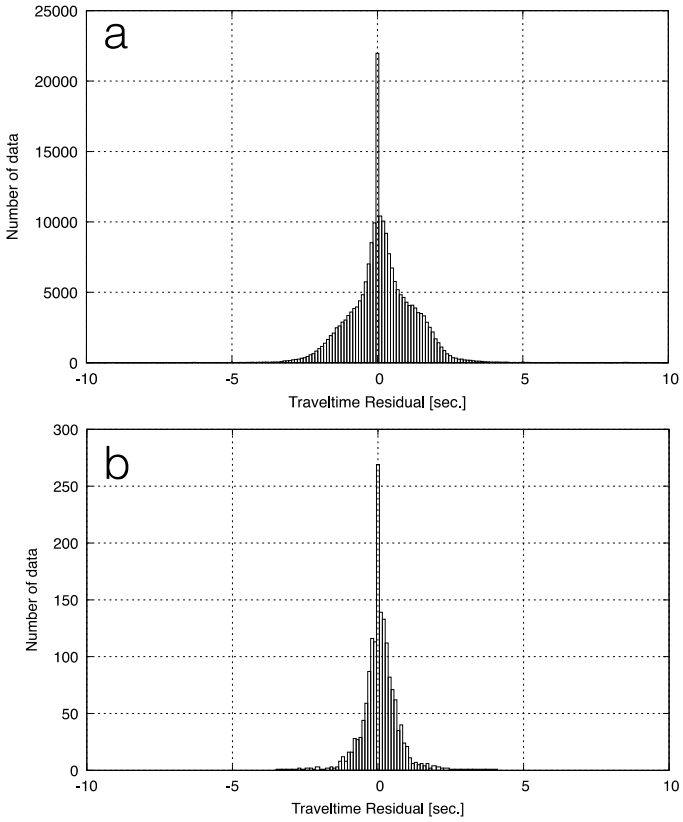

Figure 3. Histograms showing traveltime residuals between the measured traveltimes from the broadband seismograms and the theoretical traveltimes calculated with the initial one-dimensional velocity model. The initial one-dimensional model was derived through tomographic inversion using only ISC global data, involving the averaging of three-dimensional structures at each depth. The total number of (a) relative and (b) absolute traveltime data is approximately 220,000 and 1,600, respectively.

3 Methods

The tomographic inversion method followed Obayashi et al. (2013) and was based on Inoue et al. (1990). Starting from the initial model, the following steps were repeated until convergence was achieved: (1) relocation of all events; (2) calculation of traveltime residuals; (3) back-projection of traveltime residuals to the slowness perturbation model; and (4) refinement of the one-dimensional velocity model by spherical averaging of the slowness perturbations.

The seismic velocity structure of the entire mantle was parameterized using a block model that divided the mantle into latitudes, longitudes, and depths. The horizontal block size varied from 0.625° × 0.625° to 5° × 5°, which was determined such that the total length of the rays passing through each block was as uniform as possible. Additionally, the areas bounded by 30° S, 65° S, 55° W, and 80° W, which were the focus of this study, were parameterized with a minimum block size of 0.625° × 0.625°. The block configuration is illustrated in Figure S2. In the radial direction, the mantle was divided into 32 layers with thicknesses of 12, 68, and 334 km at the surface, uppermost, and bottom layers, respectively.

The initial three-dimensional P-wave velocity model was calculated by tomographic inversion using only onset time data from the ISC. Figure 3 shows the traveltime residuals of the regional datasets from the theoretical traveltime for the initial one-dimensional model obtained as the spherical average of the initial three-dimensional structures. All the events were then relocated using an initial velocity model. After relocation, traveltime residuals were calculated and back-projected onto the mantle as a slowness perturbation. In this study, we used inversion combining methods based on conventional ray theory (Inoue et al., 1990) and finite-frequency theory (Dahlen et al., 2000; Hung et al., 2000). The former approximates seismic waves with infinite frequency, whereas the latter considers frequency-dependent scattering and diffraction. Thus, the theory is valid for smaller inhomogeneities. In the ray-theoretical method, traveltime residual δT is a linear integral along the ray l as follows:

$$\delta T = \int \Delta s dl \quad (1)$$

where Δs is the slowness perturbation. Because δT is sensitive to only velocity heterogeneity along the ray path, the computation cost is very low. In contrast, finite-frequency theory gives traveltime residual as a three-dimensional volume integral as follows:

$$\delta T = \iiint \frac{\Delta s}{\bar{s}} \, K \, dq_1 dq_2 dl \quad (2)$$

where q_1, q_2 are the coordinates perpendicular to the ray-path. K is the finite-frequency sensitivity kernel, which represents the sensitivity of the δT to three-dimensional mantle structure $\Delta s/\bar{s}$. This finite-frequency sensitivity kernel is like a "Banana–Doughnut" shape: sensitive in a region surrounding the unperturbed ray path and insensitive on the ray. Because the width of the sensitivity kernel depends on the wave frequency, this method can constrain the size of heterogeneity using traveltime data measured in different frequency bands. The differential traveltime residual is as follows: $\delta(\Delta T) = \delta(\Delta T_B - \Delta T_A)$, where ΔT_A and ΔT_B are traveltime residuals calculated by Equation 2 at different stations A and B, respectively. The differential sensitivity kernel K^{B-A} is the difference between the kernels for individual stations (Hung et al., 2000). In this case, the differential kernel has strong sensitivity only directly below the station and is unaffected by the structure near the source because the overlapping parts of the two kernels are canceled out by subtraction. Sensitivity kernels were calculated using the method described by Dahlen et al. (2000).

The equation of the back-projection of traveltime residuals is as follows:

$$\begin{pmatrix} \mathbf{G} \\ \mathbf{D} \end{pmatrix} \delta \mathbf{m} = \begin{pmatrix} \delta \mathbf{d} \\ -\mathbf{D}\mathbf{m_0} \end{pmatrix} \quad (3)$$

where $\mathbf{G}$ is the data kernel, $\mathbf{D}$ is the smoothness kernel, $\delta \mathbf{m}$ is the improvement of the slowness perturbation model vector, $\mathbf{m_0}$ is the initial model, and $\delta \mathbf{d}$ is the traveltime residual vector. A first-order smoothness prior was imposed. Solving this equation using the least-squares conjugate gradient method yielded a new three-dimensional model. The L2 norm Π to be minimized for Equation 3 is as follows:

$$\Pi = \sum_i \frac{1}{\sigma_i^2} \left(t_i^{obs} - \mathrm{t}_i^{1\mathrm{D}} - \sum_k \Delta s_k l_{ik} \right)^2 + \sum_j \frac{1}{\sigma_j^2} \left(t_j^{obs} - \mathrm{t}_j^{1\mathrm{D}} - \sum_k \frac{\Delta s_k}{\bar{s}} \, K_{jk} \, V_k \right)^2 + \sum_V \left[\frac{1}{\sigma_h^2} \left(\frac{\Delta S_\theta}{r \Delta \theta} \, \Delta m_\theta^2 + \frac{\Delta S_\phi}{r \Delta \phi \, sin\theta} \, \Delta m_\phi^2 \right) + \frac{1}{\sigma_v^2} \frac{\Delta S_r}{\Delta r} \, \Delta m_r^2 \right] \quad (4)$$

where i and j are the index of residuals and k is the block index. l is the length of the ray path

segments, and V is the volume of each block. $\Delta\theta, \Delta\phi$, and Δr are step widths in latitude, longitude, and radial direction, ΔS is the contact area of the adjacent blocks along the coordinate, and Δm are the differences of adjacent slowness perturbations. There are some prior parameters; σ_i and σ_i are the standard error of t_i, σ_v and σ_h are the errors of the vertical and horizontal smoothness. The first and second terms in Equation 4 fit the model parameters to the data using ray and finite-frequency theories, respectively. The third term smooths the model with roughness parameters σ_v and σ_h adopted from Obayashi et al. (2013).

The ray theoretical method was applied to the regional absolute traveltimes and onset times from the ISC bulletin, and the finite-frequency method was applied to the differential traveltimes as a function of the frequency. It is technically straightforward to jointly invert finite-frequency traveltime measurements with ray theoretical arrival times (Montelli et al., 2004). In addition, Obayashi et al. (2013) showed that the difference between models obtained using finite-frequency kernels and ray-theoretical kernels was negligible for onset times. Therefore, a high-resolution model can be obtained with a large amount of data while saving computational cost by using the ray-theoretical method for a huge amount of global traveltime and the banana–doughnut kernel for finite-frequency traveltimes for the target region.

4 Results

4.1 Checkerboard Resolution Tests

Checkerboard Resolution Tests (CRT) were performed to evaluate the resolution of the velocity structure obtained from the dataset. To examine the resolutions at different scales, two input models with horizontal pattern sizes of 2.5° × 2.5° and 5° × 5° were defined. The pattern changed vertically every three layers. Both input models were given slowness perturbations of amplitude ±2%.

The outputs for the long-wavelength structure with 5° × 5° showed that the pattern was well recovered in the continental region down to a depth of approximately 1,200 km (Figure 4a). The input anomaly amplitudes (±2%) were fully recovered from above the transition zone to approximately 1,000 km depth, indicating good amplitude recovery at all of these depths. The high-resolution region where input anomalies were well reconstructed was along the west coast at a shallow depth of 110–150 km and extended east and west with depth. The 5° × 5° pattern was well-reconstructed on the South American continent below a depth of 300 km. Smearing artifacts elongated in a northwest to southeast direction were observed in the southeast area. Reconstruction of the 2.5° × 2.5° pattern indicated that the structures beneath the western part of the continental region were well resolved (Figure 4b). The patterns did not recover well south of ~45° S and deeper than 800 km compared to the long-wavelength case. These results indicate that our model resolves velocity inhomogeneities greater than 250 km under the continent at depths as low as ~800 km.

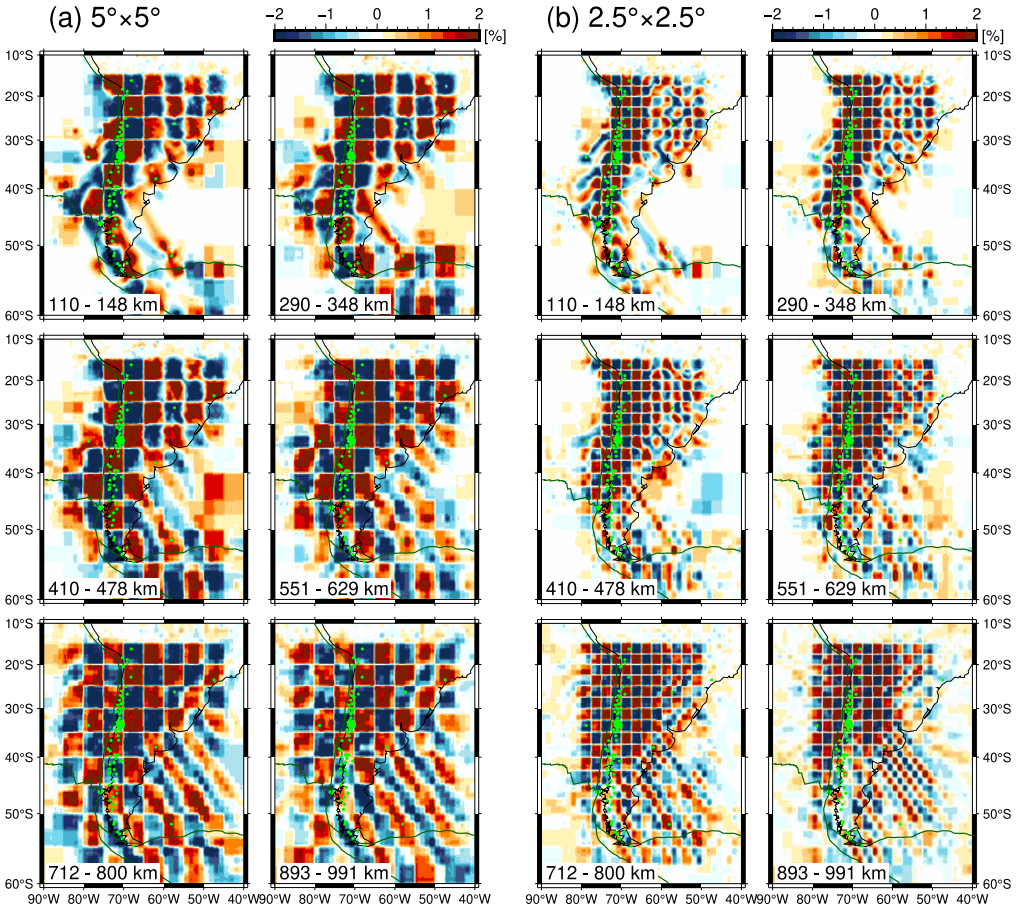

Figure 4. Output models for checkerboard resolution tests using (a) 5º × 5º and (b) 2.5º × 2.5º patterns of slowness perturbations with an amplitude of ±2%. The green dots denote seismic stations and plate boundaries are represented by dark-green lines. The slowness anomaly is presented as a percentage deviation from the one-dimensional initial velocity model.

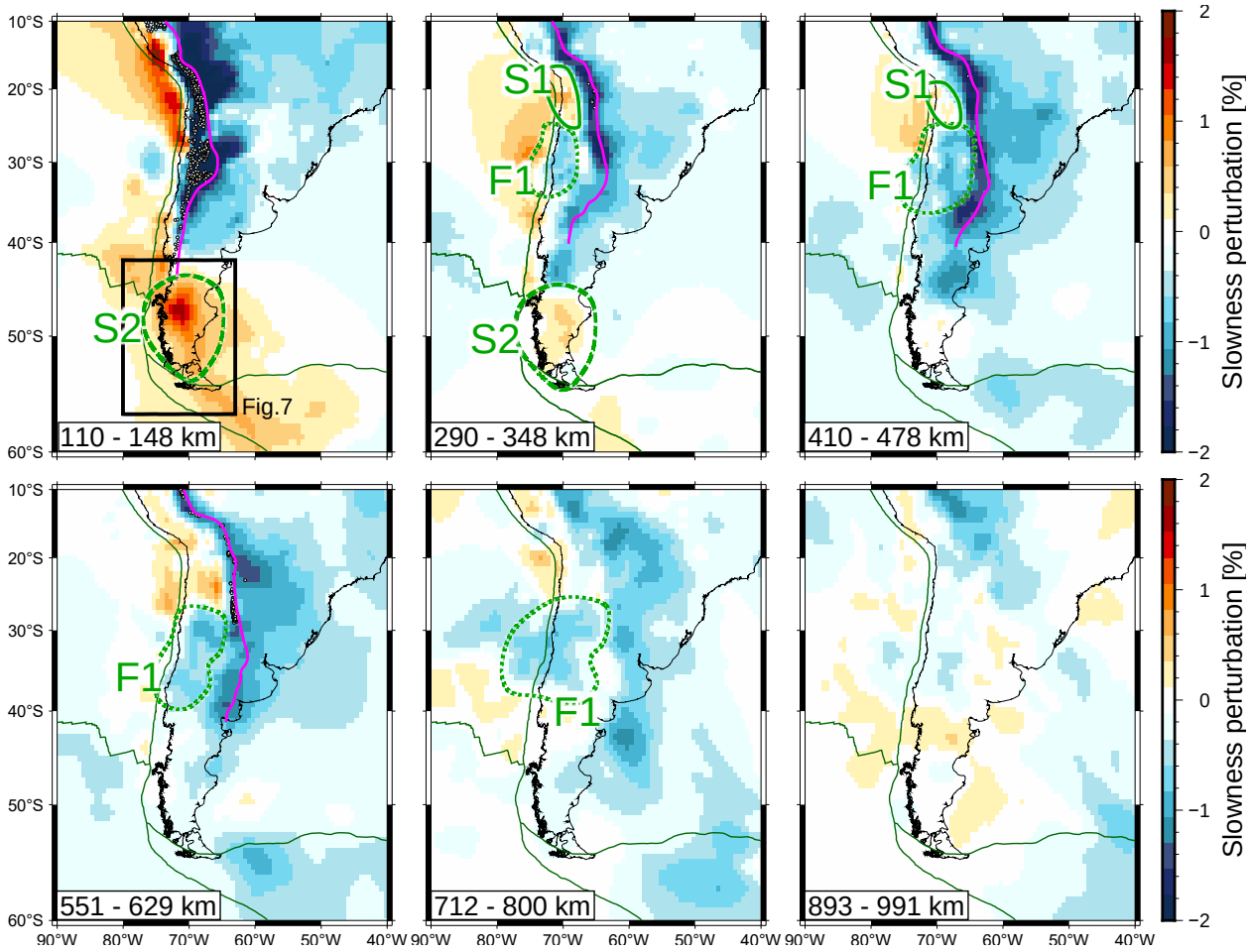

346

347 **Figure 5.** Depth slices of our final tomography model up to approximately 1,000 km depth. The
348 red color indicates slower seismic velocity anomalies relative to the spherical averaged seismic
349 velocity at each layer, while blue denotes faster anomalies. Detailed, enlarged views of the
350 vicinity of the CTJ are shown in Figure 6. Event hypocenters within each depth layer are marked
351 with white dots. The contour of the Nazca slab by the Slab2 model (Hayes et al., 2018) is
352 denoted by magenta lines. Anomalies labeled “F1,” “S1,” and “S2” are described in the text.

353

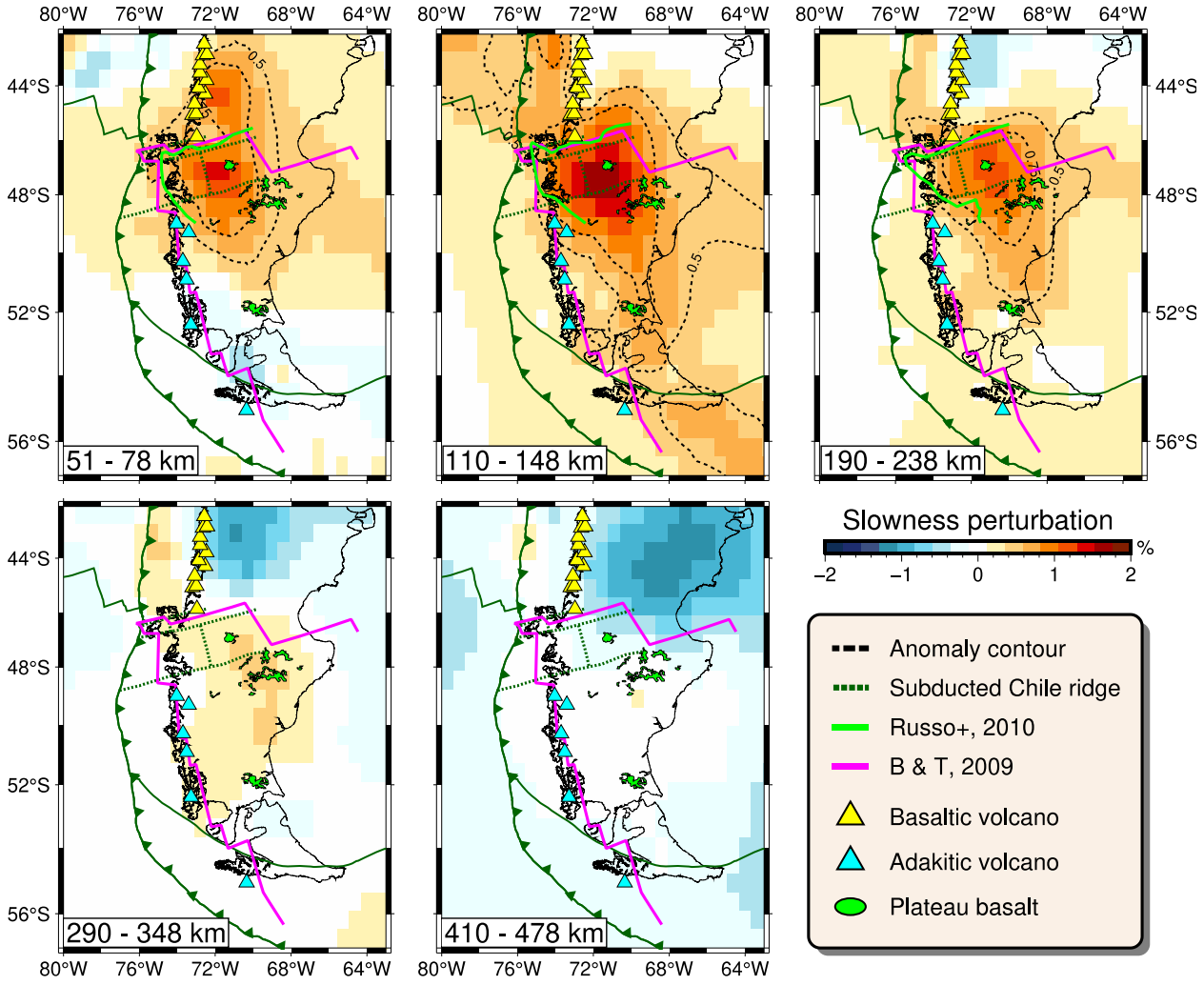

Figure 6. Result model focusing on the vicinity of CTJ (black line area in Figure 6). The black dotted lines indicate contours of a slow anomaly stronger than 0.5% in the result model, in 0.25% increments. The geometry of the Chile Ridge and associated fracture zones are projected to depth, as shown by dark-green dotted lines. Previously estimated slab windows, according to Russo et al. (2010) and Breitsprecher & Thorkelson (2009), are included for comparison.

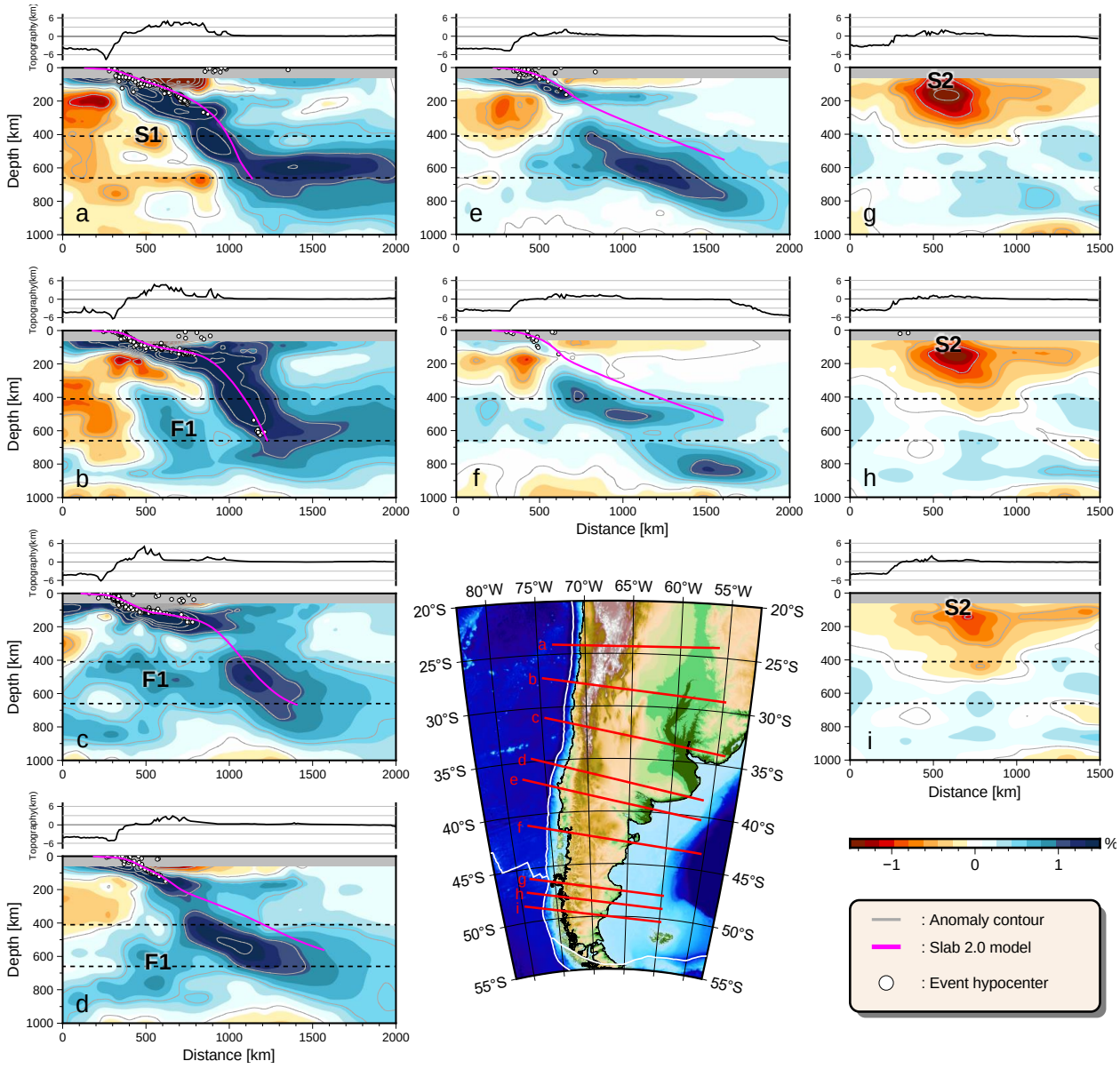

361

362 **Figure 7**. Cross sections of the resulting model approximately perpendicular to the trench strike
363 along a–i are delineated in the map. Two black dashed lines represent the 410 and 660 km
364 seismic discontinuities, respectively. White dots denote the hypocenters of seismic events. The
365 top surface of the subducting Nazca slab of the Slab2 model (Hayes et al., 2018) is denoted by
366 magenta lines. The topography along the profile is shown above each cross-section. Anomalies
367 "F1," "S1," and "S2" are labeled following the text.

368

369 ***4.2 Tomography Model***

370 The horizontal and cross sections of our final tomography model are shown in Figures 5–
371 7. These figures represent slowness perturbations in percentages, which are the residuals of the
372 average slowness at each depth layer divided by the spherical average slowness. The traveltime

data measured using the regional data revealed detailed structures of the region from latitudes of 25° S to ~55° S. (Figure S3).

The most notable structure in the northern part is the fast anomalies extending in a north-south direction. These fast anomalies are consistent with the Wadati–Benioff zone in the upper mantle and the geometry of the Chile Trench and thus can be interpreted as the subducted Nazca slab. In the upper mantle, the Nazca slab anomaly is relatively narrow, with a horizontal width of less than 200 km perpendicular to the trench. Up to a depth of 1,000 km, the slab was continuously observed as a region where the negative slowness perturbation was approximately 0.65% or stronger. These anomalies shift eastward with increasing depth and can be interpreted as cold lithospheric subduction at a certain dip angle. At 37–40º S between the depths of 150 and 300 km, the fast anomaly is weakened, as if the slab breaks off (Figure 7e). These local decreases in the slab anomaly amplitude are considered to be mainly attributed to the low resolution due to lack of the ray paths. In addition, no strong, fast anomaly was observed south of 40° S at the expected slab position shallower than 200 km, whereas it was continuously resolved on the deeper side (Figure 7f). This can be attributed to the low seismicity and few stations in the southern part and/or to the fact that the slab is very young and relatively warm. The pattern of slab subduction varied significantly along the trench. At latitudes of 20°–26° S, the slab subducts at a constant dip angle (approximately 15°–20°) from the Chile Trench to the mantle transition zone and is stagnant horizontally for more than 1,000 km in the mantle transition zone. In contrast, in the range of 28°–32° S, the slab lies horizontally for more than 300 km at a depth of approximately 130 km and then abruptly subducts with a larger dip angle. Further south, no slab bending associated with flat subduction was observed. These features are consistent with those of previous studies on the Nazca slab geometry (Ciardelli et al., 2022; Mohammadzaheri et al., 2021; Portner et al., 2020).

Three prominent strong anomalies were observed around the subducted Nazca slab: (1) slow anomalies between 20° and 32° S in the mantle transition zone (S1 in Figure 5), (2) fast anomalies beneath the Nazca slab at depths of 300–800 km between 26° and 35° S (F1 in Figure 5), and (3) strong slow anomalies on the eastern side of the CTJ (S2 in Figure 5). The location of the S1 anomalies is generally consistent with Portner et al. (2017), who interpreted the slow anomalies as a warm asthenospheric mantle derived from a hotspot entrained by Nazca plate motion, although the S1 anomalies were weaker and narrower.

The F1 anomalies are approximately parallel to the bottom of the Nazca slab; however, the deeper and southern parts of the F1 anomalies approach the Nazca slab, and their separation becomes unclear. The amplitude was less than that of the Nazca slab anomaly at all depths, with a maximum amplitude of 1.06% at the top of the mantle transition zone at 28.5° S. In the upper part of the transition zone, F1 extended 800 km along the trench direction, with an approximate width of 300 km. It extended to the south, reaching a north-south length of 1,200 km just below the transition zone. These large fast anomalies have been observed in prior teleseismic studies, with amplitudes equal to or slightly weaker than those of the Nazca slab (Pesicek et al., 2012; Portner et al., 2020), but there are discrepancies in their distributions. Pesicek et al. (2012) observed weak (~1.0%) fast anomalies from 37° S to 40° S at depths ranging from 200 to 800 km, whereas Portner et al. (2020) showed strong (~2.0–3.0%) fast anomalies from 24° S (depths of 300–800 km) to 38° S (depths of 500–1,000 km).

In the vicinity of the CTJ, notably slow anomalies (S2 in Figures 5 and 7g–i) were observed, with a maximum perturbation of 1.6% at ~48° S in a depth slice of 110–148 km. These

anomalies were bounded on the west side by the trench and extended southeast to 54° S with a gradually decreasing amplitude. The region of strong anomalies shifts eastward with depth, suggesting that S2 dips eastward. S2 was observed continuously up to a depth of 350 km. Based on its location, S2 can be interpreted as a slow anomaly associated with a Patagonian slab window. S2 is generally consistent with previous studies of regional teleseismic P-wave tomography near the CTJ (Miller et al., 2023; Russo et al., 2010) and a recent Rayleigh wave dispersion analysis (Mark et al., 2022). Active adakitic volcanism (Stern & Kilian, 1996) is located at the southern edge of S2. As noted above, the Nazca slab, which was expected to be on the north side of the slab window, was imaged as a less anomalous region surrounded by slow anomalies to the west and south. The southern side of S2 (48°–52° S), the Antarctic slab, which is expected to exist up to a depth of 45 km (Breitsprecher & Thorkelson, 2009), was not clearly represented in the resulting velocity model. Although weak fast anomalies were observed at a depth of 50 km, we did not interpret them because of low ray path coverage and weak amplitude.

4.3 Synthetic Recovery Tests

In addition to checkerboard resolution analysis, we performed synthetic recovery tests in which synthetic structures were reconstructed to examine how well the given structures were recovered using the dataset used in this study. Synthetic P-wave traveltime and differential traveltime data of all event-station pairs used in the tomographic inversion were calculated for the given test structures and then inverted to recover the test model. This test was applied to assess the reliability of three notable structures: the Nazca slab, the subslab fast anomaly (F1), and the slow anomaly associated with the Patagonian slab window (S2).

The first synthetic recovery test was conducted on a Nazca slab. Based on the resulting velocity model, we constructed synthetic fast anomaly structures for the Nazca slab, in which a uniform fast anomaly of 2% was given. The recovered model is shown in Figure 8a. The geometry of the fast anomalies in the recovered model was in accordance with that of the test model, although the recovered intensity varied regionally. North of 30° S, approximately 100% of the amplitude of the input slab model was recovered at all depths. South of 30° S, the recovered amplitude was smaller than that of the input model at a depth range of 200–400 km and in the lowermost mantle transition layer. The results of this test and the CRT suggest that the abrupt decrease in the fast anomaly intensity of the Nazca slab to the south of 30° S reflects poor resolution, whereas the configuration of the Nazca slab is well-constrained. Furthermore, weak, slow anomalies appeared around the slab, indicating that caution should be exercised when interpreting low-velocity anomalies with small amplitudes around slabs.

Another synthetic test was performed to examine the resolution of subslab fast anomalies (F1). The input model was constructed by adding fast subslab anomalies to the synthetic Nazca slab used in the previous recovery test. We tested two different subslab fast anomalies with amplitudes of 2%, which were the same as those of the synthetic Nazca slab and 1% (Figures 8b and c). In both cases, the shape and amplitude of the input subslab anomalies recovered well, indicating that the intensity of the F1 anomalies was significantly lower than that of the Nazca slab at the same latitude. Slow anomalies appeared between the Nazca slab and F1 in the recovered models, suggesting that those in the resulting model were artifacts.

Synthetic recovery tests were also conducted to slow anomalies associated with the slab window. The synthetic slab window was defined based on areas with slowness perturbations greater than the thresholds in each layer (0.7% in the shallowest layer and 0.3% in the deepest

layer at a depth of 350 km) in the resulting model and assigned a slow anomaly of 3%. To assess the depth of the slow anomalies, we created three input models with different bottom depths (approximately 150, 240, and 350 km) of slow anomalies. The recovered models showed a smearing of up to two layers from the bottom of the given slow anomalies in all cases, indicating that the actual vertical extent of the structure could be shallower than the deepest layer of the resulting model (Figure 9). Our final tomographic model best matched the model recovered from input anomalies down to 240 km. In addition, the horizontal spread of the slow anomalies was tested using two different input models (Figure S4). One was the maximum distribution, based on the slab window predicted by the plate reconstruction model (Breitsprecher & Thorkelson, 2009), and the other was the minimum extent, based on a slow area at a depth of 110 km in the resulting velocity model. The amplitude of the input velocity anomaly was 3% in both cases. The western and north-south extents were well constrained for the most part, but the eastern edge could not be constrained because of the lack of stations to the east.

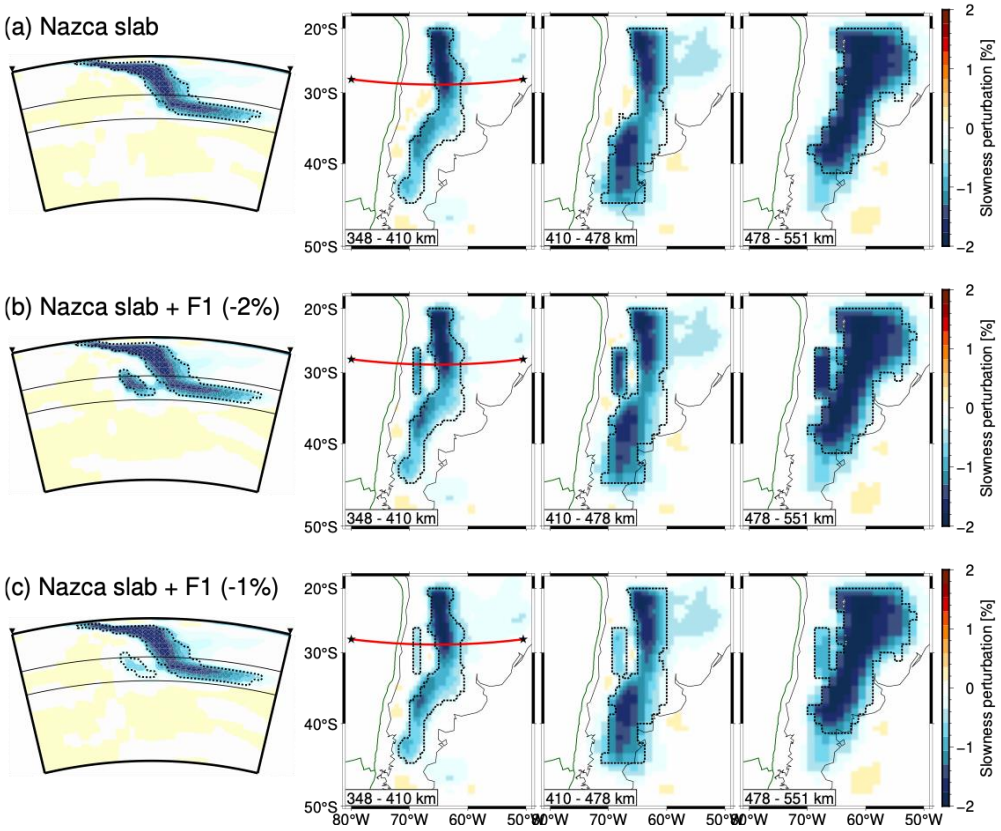

Figure 8. Results of synthetic anomaly recovery tests for Nazca slab and subslab fast anomaly. The traces for cross sections are shown as a red line in the left map. These tests are for (a) Nazca slab anomaly (2%), (b) Nazca slab anomaly (2%) with F1 anomaly (2%), and (c) Nazca slab anomaly (2%) with F1 anomaly (1%). The dotted black line outlines the input uniform anomalies in all panels.

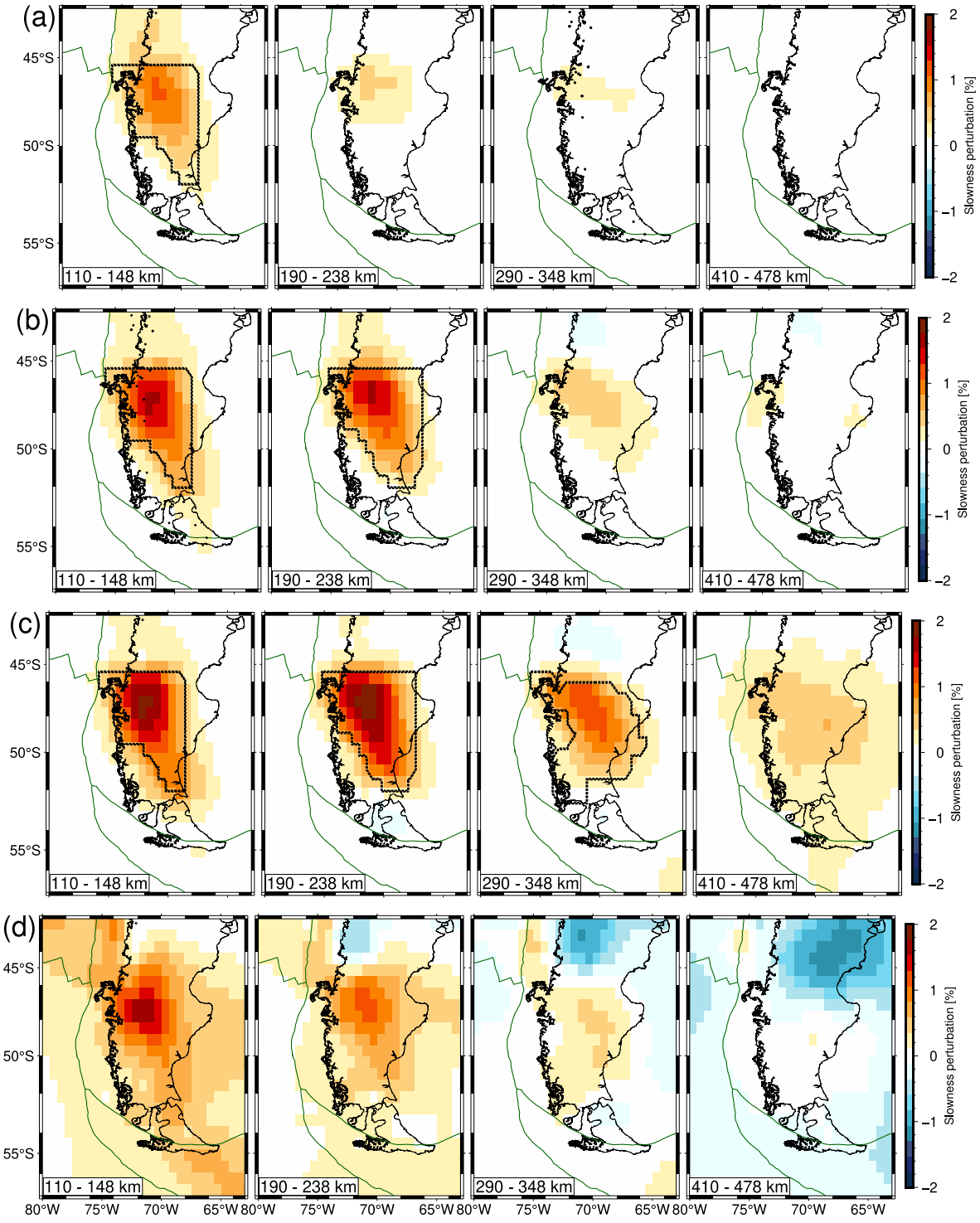

Figure 9. Results of synthetic anomaly recovery test for the vertical smearing of S2 anomaly for alternate depth layers. Tests are conducted for slow anomalies with an amplitude of 3% up to a depth of approximately (a) 150 km, (b) 250 km, and (c) 350 km. In (a)–(c) panels, the dotted black line outlines the input anomaly. (d) For comparison, the final tomography model is in the same horizontal section.

5 Discussions

5.1 Subslab Fast Anomaly Beneath the Nazca Slab

An evident high-velocity anomaly (F1) was observed beneath the Nazca slab between 26° and 35° S (Figures 5, 7b–d, and 10b). F1 is isolated from the Nazca slab fast anomaly and extends to depths of 300–900 km between the latitudes of 26–33° S, where the flat Nazca slab is located, although it approaches the Nazca slab southward. South of 33° S, in the region of normal Nazca slab subduction, F1 is situated in and below the transition zone and gradually becomes one with the Nazca slab. The amplitudes of the F1 anomalies were smaller than those of the Nazca slab anomalies over the entire F1 range. Such fast anomalies beneath the Nazca slab have been observed in previous global and regional tomographic studies, albeit with varying sizes, geometries, and amplitudes (Amaru, 2007; Li et al., 2008; Mohammadzaheri et al., 2021; Pesicek et al., 2012; Portner et al., 2017; Scire et al., 2017; Simmons et al., 2012).

Recently, several interpretations have been proposed for the F1-like fast anomalies. Rodríguez et al. (2020) found a fast anomaly beneath the Chile Trench in the latitude range of 25–35° S, with a depth of 200–1,000 km, using teleseismic shear wave tomography, and attributed it to a remnant of the Phoenix slab that was detached and stagnated in the mantle transition zone. Gao et al. (2021) estimated the S-wave velocity structure in the upper mantle through full waveform inversion and detected a high-velocity anomaly at a depth range of 200–350 km at locations similar to F1. They interpreted this anomaly as a fossil fragment of the Nazca slab that subducted steeply before the onset of flattening. They also argued that it is not appropriate to interpret this anomaly as a relic of the Phoenix plate, which was completely subducted by the Late Cretaceous (Gianni et al., 2018; Horton, 2018). Our model suggests that F1 corresponds to a detached segment of the Nazca slab associated with flat slab subduction for several reasons.

The range of F1 values observed in the resulting model was in good agreement with the locations of the current and past flat-slab segments. The northern edge of F1 (~26° S) is consistent with the Pampean flat-slab segment, which has been flat since 12Ma when the Juan Fernández Ridge was subducted (Horton, 2018). South of the current Pampean segment, the magmatic distribution, tectonic evolution, and structure of the overriding plate indicate that flat-slab subduction (Payenia flat slab) occurred from 13 to 5 Ma but is currently subducting relatively steeply (Ramos & Folguera, 2009). Although the eastern edge of the current downgoing slab in this region is still debated, it is continuous to at least ~60° W in our resulting model. The coincidence of the locations between the F1 anomaly and flat slabs indicates that the F1 anomaly may have been the relic Nazca slab that detached when slab flattening occurred (12–13Ma).

Slab break-off associated with the flat-slab subduction process has been debated in geodynamic models for both steep-to-flat (e.g., Axen et al., 2018; Liu & Currie, 2016; 2019) and flat-to-steep (e.g., Dai et al., 2020) transitions. In the case of a steep-to-flat transition, assuming that flat subduction originates from the trench-forward fast migration of the overriding continental plate and the subduction of a buoyant oceanic plateau, the oceanic lithosphere on the continental side is under tensional stress owing to the competing effects of the dense slab and buoyant oceanic plateau. This extensional stress can lead to slab break-off, in which a dense slab segment is detached. After the break-off of a dense slab, the oceanic lithosphere with a buoyant plateau is deflected upward to a sub-horizontal position near the base of the continental

lithosphere (Liu & Currie, 2016). Flat-slab subduction is generally unstable and eventually transitions to normal (steep) subduction via slab rollback or delamination (Dai et al., 2020). Slab rollback or delamination can occur if the slab becomes denser due to eclogitization after it has existed for a sufficient time at suitable pressures and temperatures for phase change. Additionally, the partial eclogitization of an oceanic plateau before or after flat subduction may play an important role in the sinking of broke-off slab segments and their timing (Arrial & Billen, 2013; Liu & Currie, 2016, 2019).

If the slab break occurred at the beginning of the slab flattening at the Pampean and Payenia (12–13 Ma), the Nazca slab should have been at least as long as the slab had been subducted. The paleo-convergence rate between the Nazca and South America plates is estimated to be 10–12 cm/yr for the period 25–5 Ma (Cande & Leslie, 1986), while the current convergence rate is ~7 cm/yr (DeMets et al. 2010). Assuming these convergence rates, the slab length, subducted for 13M years, is 1,150–1,310 km. These values are not significantly different from the ~1,500 km long fast anomalies of the Nazca slab extending from the Chile Trench to the mantle transition zone in our model. Furthermore, the South American trench has been retreating westward over a long period, and the reconstruction model suggests that it has retreated 240 ± 50 km since 12 Ma (Liu & Currie, 2019; Schepers et al., 2017). Therefore, if the Nazca slab break-off associated with slab flattening occurred near the trench at that time and the detached slab segment subsided vertically, the slab fragment would be expected to be several hundred kilometers east of the present-day trench location. This was consistent with the location of F1 in the model.

However, the temperature difference between F1 and the Nazca slab, which is estimated from the fast anomaly intensities, does not suggest that F1 was caused by slab detachment due to the subduction of the spreading ridge. The history of subduction in this region is associated with complex tectonics, resulting primarily from spreading between the Pacific, Phoenix, Antarctic, and Farallon plates since at least 84 Ma. The Farallon–Phoenix Ridge began to subduct beneath South America at ~63 Ma, although its latitude along the trench is still under debate (Cande & Leslie, 1986). At ~27 Ma, the Farallon plate was split into the Nazca and Cocos plates. The Nazca–Phoenix Ridge continues to spread and subduct beneath South America. At ~18 Ma, the triple junction of the Nazca, Phoenix, and Antarctic plates began to subduct, and after ~10 Ma, the Nazca–Phoenix Ridge completely subducted, leaving only a triple junction between Nazca, Antarctica, and South America (Breitsprecher & Thorkelson, 2009). This tectonic history suggests that spreading ridge subduction in the F1 region extended back to at least ~50 Ma (Gianni et al., 2018).

Assuming that the anomaly amplitude is sufficiently recovered based on the results of the synthetic recovery test, the maximum amplitude of the anomaly is ~1.0% for F1 and ~2.0% for the subducted Nazca slab at F1 depth. The seismic velocity anomaly was related to the temperature anomaly using the following equation (Karato, 1993):

$$\partial T = \left(\frac{\partial ln v_0}{\partial T} - \frac{H^*}{Q\pi R}\frac{1}{T^2}\right)^{-1}\frac{\partial v}{v} \quad (5)$$

where T is temperature, v is seismic velocity, H^* is activation enthalpy, Q is a seismic quality factor and R is gas constant. In the upper part of the transition zone, a difference in velocity anomaly of 1% between the F1 and the Nazca slab corresponds to a temperature difference of approximately 210 K with $\partial ln v_0 \,/\, \partial T \;= 5.27 \times 10^5\; 1/K$ (Karato, 1993), $T = 1{,}938\; K$ (Katsura, 2022), $Q = 143$ (PREM: Dziewonski & Anderson, 1981), $H^* = 80\; KJ/mol$ (Dai &

Karato, 2009) and $R = 8.13\ J/(K \cdot mol)$. From numerical simulations, it takes ~30 Myr for the stagnant slab to warm to 200 K in the transition zone, although this time highly depends on the properties of the slab and the surrounding mantle (e.g., Motoki & Ballmer, 2015). Therefore, if F1 was a detached Phoenix plate, the amplitude of its fast anomaly should be much smaller while remaining stagnant in the transition zone for approximately 50 Myr.

Although we focused on F1 anomaly in this paper, the resulting model also resolved the geometry of the Nazca slab clearly, offering insights into its evolutionary patterns. As seen in synthetic recovery tests, the Nazca slab anomaly had a reduced amplitude toward the south due to limited ray sampling. Such changes in resolution with location should be considered; however, we may be able to speculate the noted variations in slab geometry as the proxy for variation of sunken slabs over time. The strike and subduction rates along the Chile Trench south of 20° were relatively constant, while the age of the oceanic plate becomes younger to the south. Therefore, in a simplified view, the southern cross-section represents the slab's condition after a longer period since its subduction. Figure 7d and e show that the F1 anomaly was interrupted in the upper mantle as if the slab had detached. Moreover, the lower part of the slab continued deeper to the south, giving the idea that the slab had detached and then was gradually sinking. In contrast, on the east side of the upper slab there was a horizontally lying high velocity anomalies. These were not continuous to the surface and therefore they were unlikely to be high velocity anomalies associated with cratons influences observed in the north region (Rocha et al., 2011). Although it was difficult to completely separate the horizontal smearing from the slab anomaly in our final model, these structures, together with future numerical calculations and geophysical observations, will contribute to understanding of the development of the Nazca slab.

5.2 Patagonian Slab Window

Our model showed a prominent low-velocity anomaly (S2) in the putative extension of the Patagonian slab window on the eastern side of the CTJ (Figures 6 and 10). The strongest anomaly was ~1.6% at a latitude of ~48° S and a depth of ~130 km. The center of S2 coincided with the approximate location of the spreading ridge segment between the Tres Montes and Esmeralda fracture zones (green dotted line in Figure 6). The northern and western edges of S2 are bounded by the extension of the Taitao transform fault and CTJ, respectively, which constrain the edge of the Patagonian slab window. The eastern end was not well-constrained by our model because of its low resolution, as indicated by the synthetic recovery test. Further measurements extending east of our study region would help illuminate the easten edge of the Patagonian slab window. North of ~50° S, the western edge of S2 is consistent with prior imaging and the inferred extension (Breitsprecher & Thorkelson, 2009; Mark et al., 2022; Russo et al., 2010). South of ~50° S, the southern edge of the low-velocity anomaly is farther north than that predicted by the kinematic reconstruction at depths shallower than 100 km, but is generally agrees with the prediction at depths deeper than 100 km. Considering the results of the synthetic recovery test, the resulting velocity model indicates that the low-velocity anomalies associated with the slab window are continuous up to a depth of at least 200 km and do not extend to depths greater than 300 km.

At the surface, the active adakitic volcanoes in southern Patagonia are considered to be the result of partial melting of the trailing young plate edges of a slab window margin that lines the southern edge of S2. The S2 area also agrees with the proposed volcanic gap, which suggests that there is no dehydration from the slab and that the upper mantle in this region may be highly

depleted and have a low water content (Ben-Mansour et al., 2022; Ramos & Kay, 1992). In the back-arc region, S2 covered the distribution of plateau lavas younger than 3.3 Myr. These plateau lavas originate from decompression melting of the subslab asthenosphere through the slab window (Gorring & Kay, 2001).

The anomalously slow seismic velocities observed within the Patagonian slab window have been attributed to high temperatures caused by mantle upwelling, which compensates for the window and thermal erosion of the lithospheric mantle (Mark et al., 2022). Mantle upwelling in the area of the window is supported by studies on extensive Neogene Patagonian plateau lavas (e.g., Gorring et al., 1997), and net upflow can occur through the window depending on differential density, rheology, or pressure (Thorkelson, 1996). The slow anomalies throughout S2 indicate that the slab window was filled with hot material from the deeper mantle at depths of up to 250 km. The estimated depth range of the slab window also agrees with the vertical extent of the slab gap, to which upwelling can occur in the laboratory model (Király et al., 2020). In contrast, Sanhueza et al. (2023) recently conducted a numerical modeling study on the geodynamic processes caused by ridge subduction at the CTJ and suggested that asthenospheric upflow could only occur for a short time (~2 Ma) associated with the beginning of window opening. Instead, they proposed that horizontal flow from the oceanic mantle to the continental mantle might be more efficient for temperature changes. In addition, shear wave splitting analyses showed a strong EW fast direction in the vicinity of the CTJ, indicating vigorous mantle flow through the window (Russo et al., 2010; Ben-Mansour at el., 2022). Since the Chile Ridge began to subduct at around 54˚S at 18Ma, the CTJ has been migrating northward over time. Therefore, the north-south change in the crosssections can be interpreted as a proxy for the time lapse since the ridge axis was subducted. Figures 7g–i showed that the amplitude of S2 becomes smaller to the south and gradually shifts to the east. This structure may implies that the slow anomalies are like high-temperature anomalies that were generated just after the ridge subduction and are gradually weakening, rather than like a plume from the deep mantle. It is also inferred that the mantle flow is not highly turbulent, and these interpretations are consistent with Sanhueza et al. (2023).

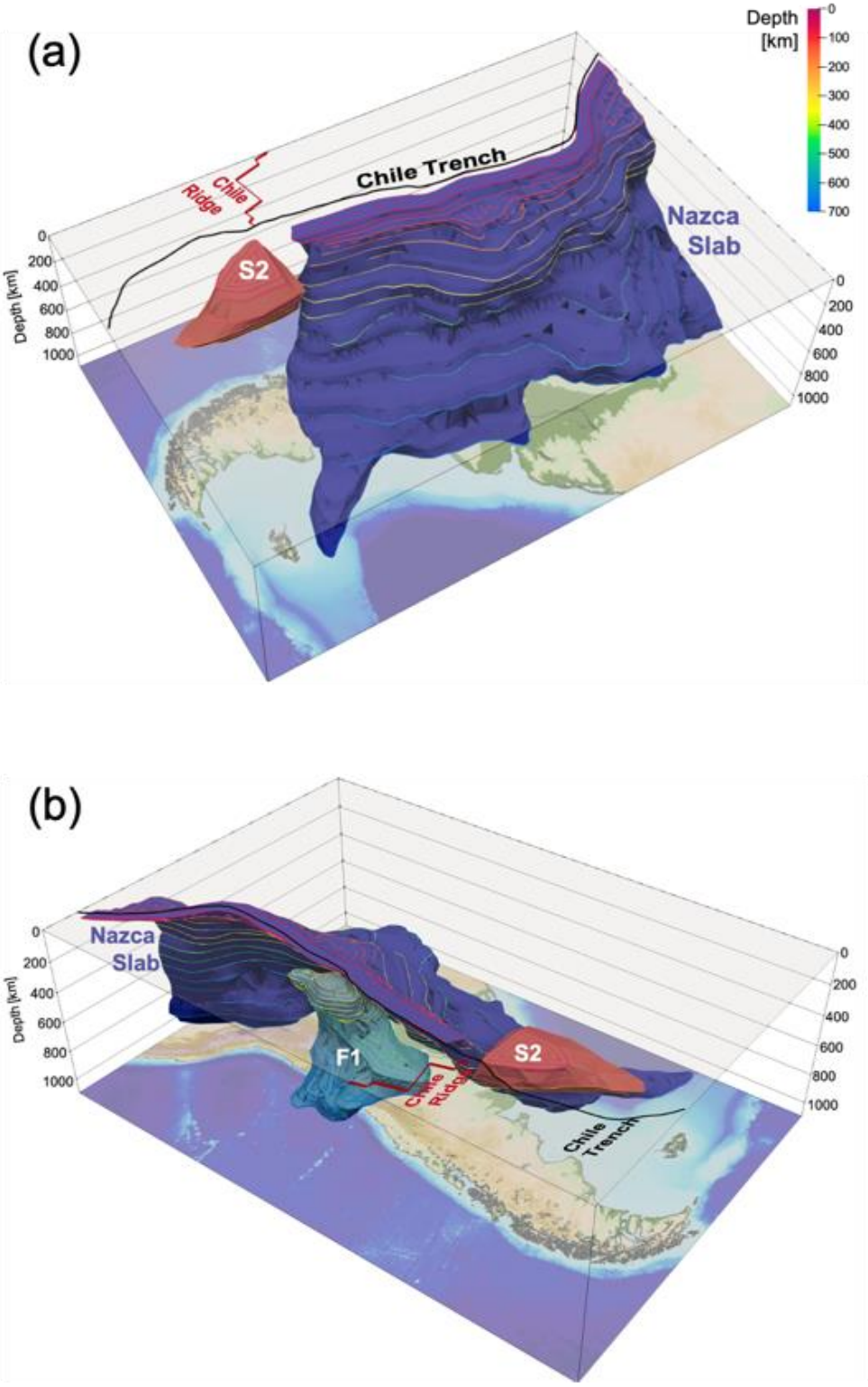

Figure 10. (a) Southeastern view and (b) southwestern view of the schematic three-dimensional image of the subducting Nazca slab and two prominent velocity anomalies interpreted in this paper from our final tomographic model. The image illustrates the interpreted Nazca slab in dark blue, the fast velocity anomaly F1 beneath the Nazca slab in light blue, and the slow velocity

anomaly to the east of the CTJ in red. The areas are same as in Figure 5, and the colored lines correspond to depth.

6 Conclusions

We performed hybrid finite-frequency and ray theoretical tomography to obtain a new P-wave velocity model for Southern South America (Figure 10). Approximately 1,600 arrivals and 224 thousand differential traveltimes were picked from broadband seismic stations, including our temporal OBS arrays at the CTJ, and 31 million global traveltime data from the ISC were used for inversion. The resulting tomography image showed some notable features of the mantle structure up to the uppermost part of the lower mantle at a depth of ~1,000 km.

(1) A fast anomaly extending beneath the Nazca slab was approximately parallel to the Nazca slab between 26° and 35° S. This fast anomaly beneath the Nazca slab may be a relic of the Nazca slab associated with flat slab subduction, based on its location, geometry, and anomaly amplitude.

(2) A strong, slow anomaly on the east of the CTJ, which is consistent with the extent of the Patagonian slab window. Our model indicated that slow anomalies associated with the slab window persisted up to depths of approximately 250 km.

Acknowledgments

In this study, we used the computer systems of the Earthquake and Volcano Information Center of the Earthquake Research Institute of the University of Tokyo. We thank the IRIS Data Management Center for providing the seismograms used in this study. Genetic Mapping Tools 6.4.0 (https://www.generic-mapping-tools.org/download/), developed by Wessel et al. (2019), was used to create the figures. This work was supported by JSPS KAKENHI Grant Number 23KJ1568 for YK and 18H01304 for MK. JO acknowledges support from the Agencia Nacional de Investigación y Desarrollo (Scholarship ANID-PFCHA/Doctorado Nacional/2020-21200903).

Open Research

OBS data in the vicinity of the Chile Triple Junction are available from the Ocean Hemisphere Project Data Management Center, Earthquake Research Institute, University of Tokyo (http://ohpdmc.eri.u-tokyo.ac.jp/). Seismograms from onshore stations are available from the Incorporated Research Institutions for Seismology Data Management Center (https://ds.iris.edu/ds/nodes/dmc/).

References

Agurto-Detzel, H., Rietbrock, A., Bataille, K., Miller, M., Iwamori, H., & Priestley, K. (2014). Seismicity distribution in the vicinity of the Chile Triple Junction, Aysén Region, southern Chile. *Journal of South American Earth Sciences*, 51, 1–11. https://doi.org/10.1016/j.jsames.2013.12.011

Amaru, M. (2007). Global travel time tomography with 3-D reference models.

Antonijevic, S., Wagner, L. S., Beck, S. L., Long, M. D., Zandt, G., & Tavera, H. (2016). Effects of change in slab geometry on the mantle flow and slab fabric in Southern Peru. *Journal of Geophysical Research: Solid Earth*, 121(10), 7252–7270. https://doi.org/10.1002/2016JB013064

Arrial, P.-A., & Billen, M. I. (2013). Influence of geometry and eclogitization on oceanic plateau subduction. *Earth and Planetary Science Letters*, 363, 34–43. https://doi.org/10.1016/j.epsl.2012.12.011

Ávila, P., & Dávila, F. M. (2018). Heat flow and lithospheric thickness analysis in the Patagonian asthenospheric windows, southern South America. *Tectonophysics*, 747–748, 99–107. https://doi.org/10.1016/j.tecto.2018.10.006

Axen, G. J., van Wijk, J. W., & Currie, C. A. (2018). Basal continental mantle lithosphere displaced by flat-slab subduction. *Nature Geoscience*, 11(12), Article 12. https://doi.org/10.1038/s41561-018-0263-9

Bangs, N. L., & Cande, S. C. (1997). Episodic development of a convergent margin inferred from structures and processes along the southern Chile margin. *Tectonics*, 16(3), 489–503. https://doi.org/10.1029/97TC00494

Barazangi, M., & Isacks, B. L. (1976). Spatial distribution of earthquakes and subduction of the Nazca plate beneath South America. *Geology*, 4(11), 686–692. https://doi.org/10.1130/0091-7613(1976)4<686:SDOEAS>2.0.CO;2

Ben-Mansour, W., Wiens, D. A., Mark, H. F., Russo, R. M., Richter, A., Marderwald, E., & Barrientos, S. (2022). Mantle Flow Pattern Associated With the Patagonian Slab Window Determined From Azimuthal Anisotropy. *Geophysical Research Letters*, 49(18). https://doi.org/10.1029/2022GL099871

Bianchi, M., Heit, B., Jakovlev, A., Yuan, X., Kay, S. M., Sandvol, E., Alonso, R. N., Coira, B., Brown, L., Kind, R., & Comte, D. (2013). Teleseismic tomography of the southern Puna plateau in Argentina and adjacent regions. *Tectonophysics*, 586, 65–83. https://doi.org/10.1016/j.tecto.2012.11.016

Bourgois, J., Guivel, C., Lagabrielle, Y., Calmus, T., Boulègue, J., & Daux, V. (2000). Glacial-interglacial trench supply variation, spreading-ridge subduction, and feedback controls on the Andean margin development at the Chile triple junction area (45–48°S). *Journal of Geophysical Research: Solid Earth*, 105(B4), 8355–8386. https://doi.org/10.1029/1999JB900400

Bourgois, J., Lagabrielle, Y., Martin, H., Dyment, J., Frutos, J., & Cisternas, M. E. (2016). A Review on Forearc Ophiolite Obduction, Adakite-Like Generation, and Slab Window Development at the Chile Triple Junction Area: Uniformitarian Framework for Spreading-Ridge Subduction. *Pure and Applied Geophysics*, 173(10), 3217–3246. https://doi.org/10.1007/s00024-016-1317-9

Bourgois, J., Martin, H., Lagabrielle, Y., Le Moigne, J., & Frutos Jara, J. (1996). Subduction erosion related to spreading-ridge subduction: Taitao peninsula (Chile margin triple junction area). *Geology*, 24(8), 723. https://doi.org/10.1130/0091-7613(1996)024<0723:SERTSR>2.3.CO;2

Boutonnet, E., Arnaud, N., Guivel, C., Lagabrielle, Y., Scalabrino, B., & Espinoza, F. (2010). Subduction of the South Chile active spreading ridge: A 17Ma to 3Ma magmatic record in central Patagonia (western edge of Meseta del Lago Buenos Aires, Argentina). *Journal of Volcanology and Geothermal Research*, 189(3), 319–339. https://doi.org/10.1016/j.jvolgeores.2009.11.022

Breitsprecher, K., & Thorkelson, D. J. (2009). Neogene kinematic history of Nazca–Antarctic–Phoenix slab windows beneath Patagonia and the Antarctic Peninsula. *Tectonophysics*, 464(1–4), 10–20. https://doi.org/10.1016/j.tecto.2008.02.013

Burd, A. I., Booker, J. R., Mackie, R., Pomposiello, C., & Favetto, A. (2013). Electrical conductivity of the Pampean shallow subduction region of Argentina near 33 S: Evidence for a slab window. *Geochemistry, Geophysics, Geosystems*, 14(8), 3192–3209. https://doi.org/10.1002/ggge.20213

Cahill, T., & Isacks, B. L. (1992). Seismicity and shape of the subducted Nazca Plate. *Journal of Geophysical Research*, 97(B12), 17503–17529. https://doi.org/10.1029/92JB00493

Cande, S. C., & Leslie, R. B. (1986). Late Cenozoic tectonics of the Southern Chile Trench. *Journal of Geophysical Research*, 91(B1), 471–496. https://doi.org/10.1029/JB091iB01p00471

Cande, S. C., Leslie, R. B., Parra, J. C., & Hobart, M. (1987). Interaction between the Chile Ridge and Chile Trench: Geophysical and geothermal evidence. *Journal of Geophysical Research*, 92(B1), 495–520. https://doi.org/10.1029/JB092iB01p00495

Celli, N. L., Lebedev, S., Schaeffer, A. J., Ravenna, M., & Gaina, C. (2020). The upper mantle beneath the South Atlantic Ocean, South America and Africa from waveform tomography with massive data sets. *Geophysical Journal International*, 221(1), 178–204. https://doi.org/10.1093/gji/ggz574

Chen, Y.-W., Wu, J., & Suppe, J. (2019). Southward propagation of Nazca subduction along the Andes. *Nature*, 565, 441–447. https://doi.org/10.1038/s41586-018-0860-1

Ciardelli, C., Assumpção, M., Bozdağ, E., & van der Lee, S. (2022). Adjoint Waveform Tomography of South America. *Journal of Geophysical Research: Solid Earth*, 127, e2021JB022575. https://doi.org/10.1029/2021JB022575

Cristallini, E. O., & Ramos, V. A. (2000). Thick-skinned and thin-skinned thrusting in the La Ramada fold and thrust belt: Crustal evolution of the High Andes of San Juan, Argentina (32°SL). *Tectonophysics*, 317, 205–235. https://doi.org/10.1016/S0040-1951(99)00276-0

763 Dahlen, F. A., Hung, S.-H., & Nolet, G. (2000). Fréchet kernels for finite-frequency
764 traveltimes-I. Theory. *Geophysical Journal International*, 141(1), 157–174.
765 https://doi.org/10.1046/j.1365-246X.2000.00070.x

766 Dai, L., & Karato, S. (2009). Electrical conductivity of wadsleyite at high temperatures
767 and high pressures. *Earth and Planetary Science Letters*, 287(1–2), 277–283.
768 https://doi.org/10.1016/j.epsl.2009.08.012

769 Dai, L., Wang, L., Lou, D., Li, Z.-H., Dong, H., Ma, F., Li, F., Li, S., & Yu, S. (2020).
770 Slab Rollback Versus Delamination: Contrasting Fates of Flat-Slab Subduction and Implications
771 for South China Evolution in the Mesozoic. *Journal of Geophysical Research: Solid Earth*,
772 125(4), e2019JB019164. https://doi.org/10.1029/2019JB019164

773 Dávila, F. M., & Lithgow-Bertelloni, C. (2013). Dynamic topography in South America.
774 *Journal of South American Earth Sciences*, 43, 127–144.
775 https://doi.org/10.1016/j.jsames.2012.12.002

776 DeLong, S. E., Schwarz, W. M., & Anderson, R. N. (1979). Thermal effects of ridge
777 subduction. *Earth and Planetary Science Letters*, 44(2), 239–246. https://doi.org/10.1016/0012-
778 821X(79)90172-9

779 DeMets, C., Gordon, R. G., & Argus, D. F. (2010). *Geologically current plate motions.*
780 *Geophysical Journal International*, 181(1), 1–80. https://doi.org/10.1111/j.1365-
781 246X.2009.04491.x

782 Dickinson, W. R., & Snyder, W. S. (1979). Geometry of Subducted Slabs Related to San
783 Andreas Transform. *The Journal of Geology*, 87(6), 609–627. https://doi.org/10.1086/628456

784 Dziewonski, A. M., & Anderson, D. L. (1981). Preliminary reference Earth model.
785 *Physics of the Earth and Planetary Interiors*, 25(4), 297–356. https://doi.org/10.1016/0031-
786 9201(81)90046-7

787 Eagles, G., Gohl, K., & Larter, R. D. (2009). Animated tectonic reconstruction of the
788 Southern Pacific and alkaline volcanism at its convergent margins since Eocene times.
789 *Tectonophysics*, 464(1–4), 21–29. https://doi.org/10.1016/j.tecto.2007.10.005

790 Espinoza, F., Morata, D., Pelleter, E., Maury, R. C., Suárez, M., Lagabrielle, Y., Polvé,
791 M., Bellon, H., Cotten, J., De la Cruz, R., & Guivel, C. (2005). Petrogenesis of the Eocene and
792 Mio–Pliocene alkaline basaltic magmatism in Meseta Chile Chico, southern Patagonia, Chile:
793 Evidence for the participation of two slab windows. *Lithos*, 82(3), 315–343.
794 https://doi.org/10.1016/j.lithos.2004.09.024

795 Espurt, N., Funiciello, F., Martinod, J., Guillaume, B., Regard, V., Faccenna, C., &
796 Brusset, S. (2008). Flat subduction dynamics and deformation of the South American plate:
797 Insights from analog modeling. *Tectonics*, 27(3). https://doi.org/10.1029/2007TC002175

798 Feng, M., van der Lee, S., & Assumpção, M. (2007). Upper mantle structure of South
799 America from joint inversion of waveforms and fundamental mode group velocities of Rayleigh
800 waves. *Journal of Geophysical Research: Solid Earth*, 112, B04312.
801 https://doi.org/10.1029/2006JB004449

802 Forsythe, R. D., Nelson, E. P., Carr, M. J., Kaeding, M. E., Herve, M., Mpodozis, C.,
803 Soffia, J. M., & Harambour, S. (1986). Pliocene near-trench magmatism in southern Chile: A

804 possible manifestation of ridge collision. *Geology*, 14(1), 23–27. https://doi.org/10.1130/0091-
805 7613(1986)14<23:PNMISC>2.0.CO;2

806 Gallego, A., Russo, R. M., Comte, D., Mocanu, V. I., Murdie, R. E., & Vandecar, J. C.
807 (2010). Seismic noise tomography in the Chile ridge subduction region: Seismic noise recorded
808 in the CTJ. *Geophysical Journal International*, 182(3), 1478–1492.
809 https://doi.org/10.1111/j.1365-246X.2010.04691.x

810 Gao, Y., Yuan, X., Heit, B., Tilmann, F., van Herwaarden, D.-P., Thrastarson, S.,
811 Fichtner, A., & Schurr, B. (2021). Impact of the Juan Fernandez Ridge on the Pampean Flat
812 Subduction Inferred From Full Waveform Inversion. *Geophysical Research Letters*, 48,
813 e2021GL095509. https://doi.org/10.1029/2021GL095509

814 Gianni, G. M., Pesce, A., & Soler, S. R. (2018). Transient plate contraction between two
815 simultaneous slab windows: Insights from Paleogene tectonics of the Patagonian Andes. *Journal*
816 *of Geodynamics*, 121, 64–75. https://doi.org/10.1016/j.jog.2018.07.008

817 Gorring, M. L., & Kay, S. M. (2001). Mantle Processes and Sources of Neogene Slab
818 Window Magmas from Southern Patagonia, Argentina. *Journal of Petrology*, 42(6), 1067–1094.
819 https://doi.org/10.1093/petrology/42.6.1067

820 Gorring, M. L., Kay, S. M., Zeitler, P. K., Ramos, V. A., Rubiolo, D., Fernandez, M. I.,
821 & Panza, J. L. (1997). Neogene Patagonian plateau lavas: Continental magmas associated with
822 ridge collision at the Chile Triple Junction. *Tectonics*, 16(1), 1–17.
823 https://doi.org/10.1029/96TC03368

824 Groome, W. G., & Thorkelson, D. J. (2009). The three-dimensional thermo-mechanical
825 signature of ridge subduction and slab window migration. *Tectonophysics*, 464, 70–83.
826 https://doi.org/10.1016/j.tecto.2008.07.003

827 Guillaume, B., Martinod, J., Husson, L., Roddaz, M., & Riquelme, R. (2009). Neogene
828 uplift of central eastern Patagonia: Dynamic response to active spreading ridge subduction?
829 *Tectonics*, 28(2), TC2009. https://doi.org/10.1029/2008TC002324

830 Guillaume, B., Moroni, M., Funiciello, F., Martinod, J., & Faccenna, C. (2010). Mantle
831 flow and dynamic topography associated with slab window opening: Insights from laboratory
832 models. *Tectonophysics*, 496(1), 83–98. https://doi.org/10.1016/j.tecto.2010.10.014

833 Gutiérrez, F., Gioncada, A., González Ferran, O., Lahsen, A., & Mazzuoli, R. (2005).
834 The Hudson Volcano and surrounding monogenetic centres (Chilean Patagonia): An example of
835 volcanism associated with ridge–trench collision environment. *Journal of Volcanology and*
836 *Geothermal Research*, 145(3–4), 207–233. https://doi.org/10.1016/j.jvolgeores.2005.01.014

837 Gutscher, M.-A., Spakman, W., Bijwaard, H., & Engdahl, E. R. (2000). Geodynamics of
838 flat subduction: Seismicity and tomographic constraints from the Andean margin. *Tectonics*,
839 19(5), 814–833. https://doi.org/10.1029/1999TC001152

840 Hayes, G. P., Moore, G. L., Portner, D. E., Hearne, M., Flamme, H., Furtney, M., &
841 Smoczyk, G. M. (2018). Slab2, a comprehensive subduction zone geometry model. *Science*,
842 362(6410), 58–61. https://doi.org/10.1126/science.aat4723

Horton, B. K. (2018). Tectonic Regimes of the Central and Southern Andes: Responses to Variations in Plate Coupling During Subduction. *Tectonics*, 37(2), 402–429. https://doi.org/10.1002/2017TC004624

Hung, S.-H., Dahlen, F. A., & Nolet, G. (2000). Fréchet kernels for finite-frequency traveltimes-II. Examples. *Geophysical Journal International*, 141(1), 175–203. https://doi.org/10.1046/j.1365-246X.2000.00072.x

Inoue, H., Fukao, Y., Tanabe, K., & Ogata, Y. (1990). Whole mantle P-wave travel time tomography. *Physics of the Earth and Planetary Interiors*, 59(4), 294–328. https://doi.org/10.1016/0031-9201(90)90236-Q

Ito, A., Shiobara, H., Miller, M., Sugioka, H., Ojeda, J., Tassara, C., Shinohara, M., Kinoshita, M., & Iwamori, H. (2023). Long-term array observation by ocean bottom seismometers at the Chile Triple Junction. *Journal of South American Earth Sciences*, 124, 104285. https://doi.org/10.1016/j.jsames.2023.104285

Kaeding, M., Forsythe, R. D., & Nelson, E. P. (1990). Geochemistry of the Taitao ophiolite and near-trench intrusions from the Chile margin triple junction. *Journal of South American Earth Sciences*, 3(4), 161–177. https://doi.org/10.1016/0895-9811(90)90001-H

Karato, S. (1993). Importance of anelasticity in the interpretation of seismic tomography. *Geophysical Research Letters*, 20(15), 1623–1626. https://doi.org/10.1029/93GL01767

Karsten, J. L., Klein, E. M., & Sherman, S. B. (1996). Subduction zone geochemical characteristics in ocean ridge basalts from the southern Chile Ridge: Implications of modern ridge subduction systems for the Archean. *Lithos*, 37, 143–161. https://doi.org/10.1016/0024-4937(95)00034-8

Katsura, T. (2022). A Revised Adiabatic Temperature Profile for the Mantle. *Journal of Geophysical Research: Solid Earth*, 127(2). https://doi.org/10.1029/2021JB023562

Kay, S. M., & Coira, B. L. (2009). Shallowing and steepening subduction zones, continental lithospheric loss, magmatism, and crustal flow under the Central Andean Altiplano-Puna Plateau. In S. M. Kay, V. A. Ramos, & W. R. Dickinson, Backbone of the Americas: Shallow Subduction, Plateau Uplift, and Ridge and Terrane Collision. *Geological Society of America*. https://doi.org/10.1130/2009.1204(11)

Kay, S. M., & Mpodozis, C. (2002). Magmatism as a probe to the Neogene shallowing of the Nazca plate beneath the modern Chilean flat-slab. *Journal of South American Earth Sciences*, 15(1), 39–57. https://doi.org/10.1016/S0895-9811(02)00005-6

Kennett, B. L. N., & Engdahl, E. R. (1991). Traveltimes for global earthquake location and phase identification. *Geophysical Journal International*, 105(2), 429–465. https://doi.org/10.1111/j.1365-246X.1991.tb06724.x

Király, Á., Portner, D. E., Haynie, K. L., Chilson-Parks, B. H., Ghosh, T., Jadamec, M., Makushkina, A., Manga, M., Moresi, L., & O'Farrell, K. A. (2020). The effect of slab gaps on subduction dynamics and mantle upwelling. *Tectonophysics*, 785, 228458. https://doi.org/10.1016/j.tecto.2020.228458

Lagabrielle, Y., Guivel, C., Maury, R. C., Bourgois, J., Fourcade, S., & Martin, H. (2000). Magmatic–tectonic effects of high thermal regime at the site of active ridge subduction:

The Chile Triple Junction model. *Tectonophysics*, 326, 255–268. https://doi.org/10.1016/S0040-1951(00)00124-4

Lagabrielle, Y., Moigne, J. L., Maury, R. C., Cotten, J., & Bourgois, J. (1994). Volcanic record of the subduction of an active spreading ridge, Taitao Peninsula (southern Chile). *Geology*, 22(6), 515–518. https://doi.org/10.1130/0091-7613(1994)022<0515:VROTSO>2.3.CO;2

Li, C., van der Hilst, R. D., Engdahl, E. R., & Burdick, S. (2008). A new global model for P wave speed variations in Earth's mantle: *Geochemistry, Geophysics, Geosystems*, 9(5). https://doi.org/10.1029/2007GC001806

Liu, S., & Currie, C. A. (2016). Farallon plate dynamics prior to the Laramide orogeny: Numerical models of flat subduction. *Tectonophysics*, 666, 33–47. https://doi.org/10.1016/j.tecto.2015.10.010

Liu, X., & Currie, C. A. (2019). Influence of Upper Plate Structure on Flat-Slab Depth: Numerical Modeling of Subduction Dynamics. *Journal of Geophysical Research: Solid Earth*, 124(12), 13150–13167. https://doi.org/10.1029/2019JB018653

Lu, C., Grand, S. P., Lai, H., & Garnero, E. J. (2019). TX2019slab: A New P and S Tomography Model Incorporating Subducting Slabs. *Journal of Geophysical Research: Solid Earth*, 124(11), 11549–11567. https://doi.org/10.1029/2019JB017448

Maksymowicz, A., Contreras-Reyes, E., Grevemeyer, I., & Flueh, E. R. (2012). Structure and geodynamics of the post-collision zone between the Nazca–Antarctic spreading center and South America. *Earth and Planetary Science Letters*, *345*, 27-37. https://doi.org/10.1016/j.epsl.2012.06.023

Manea, V. C., Manea, M., Ferrari, L., Orozco-Esquivel, T., Valenzuela, R. W., Husker, A., & Kostoglodov, V. (2017). A review of the geodynamic evolution of flat slab subduction in Mexico, Peru, and Chile. *Tectonophysics*, 695, 27–52. https://doi.org/10.1016/j.tecto.2016.11.037

Manea, V. C., Pérez-Gussinyé, M., & Manea, M. (2012). Chilean flat slab subduction controlled by overriding plate thickness and trench rollback. *Geology*, 40(1), 35–38. https://doi.org/10.1130/G32543.1

Mark, H. F., Wiens, D. A., Ivins, E. R., Richter, A., Ben Mansour, W., Magnani, M. B., Marderwald, E., Adaros, R., & Barrientos, S. (2022). Lithospheric Erosion in the Patagonian Slab Window, and Implications for Glacial Isostasy. *Geophysical Research Letter*s, 49, e2021GL096863. https://doi.org/10.1029/2021GL096863

Marot, M., Monfret, T., Gerbault, M., Nolet, G., Ranalli, G., & Pardo, M. (2014). Flat versus normal subduction zones: A comparison based on 3-D regional traveltime tomography and petrological modelling of central Chile and western Argentina (29°–35°S). *Geophysical Journal International*, 199(3), 1633–1654. https://doi.org/10.1093/gji/ggu355

Martinod, J., Guillaume, B., Espurt, N., Faccenna, C., Funiciello, F., & Regard, V. (2013). Effect of aseismic ridge subduction on slab geometry and overriding plate deformation: Insights from analogue modeling. *Tectonophysics*, 588, 39–55. https://doi.org/10.1016/j.tecto.2012.12.010

Miller, M., Priestley, K., Tilmann, F., Bataille, K., & Iwamori, H. (2023). P wave teleseismic tomography of the subducted Chile rise. *Journal of South American Earth Sciences*, 128 . https://doi.org/10.1016/j.jsames.2023.104474

Mohammadzaheri, A., Sigloch, K., Hosseini, K., & Mihalynuk, M. G. (2021). Subducted Lithosphere Under South America From Multifrequency P Wave Tomography. *Journal of Geophysical Research: Solid Earth*, 126, e2020JB020704. https://doi.org/10.1029/2020JB020704

Montelli, R., Nolet, G., Masters, G., Dahlen, F. A., & Hung, S.-H. (2004). Global P and PP traveltime tomography: Rays versus waves. *Geophysical Journal International*, 158(2), 637–654. https://doi.org/10.1111/j.1365-246X.2004.02346.x

Motoki, M. H., & Ballmer, M. D. (2015). Intraplate volcanism due to convective instability of stagnant slabs in the mantle transition zone. *Geochemistry, Geophysics, Geosystems*, 16(2), 538–551. https://doi.org/10.1002/2014GC005608

Müller, R. D., Sdrolias, M., Gaina, C., & Roest, W. R. (2008). Age, spreading rates, and spreading asymmetry of the world's ocean crust. *Geochemistry, Geophysics, Geosystems*, 9(4). https://doi.org/10.1029/2007GC001743

Murdie, R. E., Styles, P., Prior, D. J., & Daniel, A. J. (2000). A new gravity map of southern Chile and its preliminary interpretation. *Revista Geológica de Chile*, 27(1), 49–63. https://doi.org/10.4067/S0716-02082000000100004

Nelson, E., Forsythe, R., Diemer, J., Allen, M., & Urbina, O. (1993). Taitao ophiolite: A ridge eollision ophiolite in the toreare of southern Chile (460 S). Rev/Sta Geológica de Chile, 20(2), 137–165.

Obayashi, M., Yoshimitsu, J., Nolet, G., Fukao, Y., Shiobara, H., Sugioka, H., Miyamachi, H., & Gao, Y. (2013). Finite frequency whole mantle P wave tomography: Improvement of subducted slab images. *Geophysical Research Letters*, 40(21), 5652–5657. https://doi.org/10.1002/2013GL057401

Pesicek, J. D., Engdahl, E. R., Thurber, C. H., DeShon, H. R., & Lange, D. (2012). Mantle subducting slab structure in the region of the 2010 M8.8 Maule earthquake (30-40°S), Chile: Mantle subducting slab structure in Chile. *Geophysical Journal International*, 191(1), 317–324. https://doi.org/10.1111/j.1365-246X.2012.05624.x

Portner, D. E., Beck, S., Zandt, G., & Scire, A. (2017). The nature of subslab slow velocity anomalies beneath South America. *Geophysical Research Letters*, 44(10), 4747–4755. https://doi.org/10.1002/2017GL073106

Portner, D. E., Rodríguez, E. E., Beck, S., Zandt, G., Scire, A., Rocha, M. P., Bianchi, M. B., Ruiz, M., França, G. S., Condori, C., & Alvarado, P. (2020). Detailed Structure of the Subducted Nazca Slab into the Lower Mantle Derived From Continent-Scale Teleseismic P Wave Tomography. *Journal of Geophysical Research: Solid Earth*, 125, e2019JB017884. https://doi.org/10.1029/2019JB017884

Ramos, V. A. (1999). Plate tectonic setting of the Andean Cordillera. *Episodes*, 22(3), 183–190. https://doi.org/10.18814/epiiugs/1999/v22i3/005

Ramos, V. A., Cristallini, E. O., & Pérez, D. J. (2002). The Pampean flat-slab of the Central Andes. *Journal of South American Earth Sciences*, 15(1), 59–78. https://doi.org/10.1016/S0895-9811(02)00006-8

Ramos, V. A., & Folguera, A. (2009). Andean flat-slab subduction through time. *Geological Society, London, Special Publications*, 327(1), 31–54. https://doi.org/10.1144/SP327.3

Ramos, V. A., & Kay, S. M. (1992). Southern Patagonian plateau basalts and deformation: Backarc testimony of ridge collisions. *Tectonophysics*, 205(1–3), 261–282. https://doi.org/10.1016/0040-1951(92)90430-E

Rawlinson, N., & Kennett, B. L. N. (2004). Rapid estimation of relative and absolute delay times across a network by adaptive stacking. *Geophysical Journal International*, 157(1), 332–340. https://doi.org/10.1111/j.1365-246X.2004.02188.x

Rocha, M. P., Schimmel M., Assumpção M. (2011) Upper-mantle seismic structure beneath SE and Central Brazil from *P*- and *S*-wave regional traveltime tomography, *Geophysical Journal International*, 184(1), 268–286, https://doi.org/10.1111/j.1365-246X.2010.04831.x

Rodríguez, E. E., Portner, D. E., Beck, S. L., Rocha, M. P., Bianchi, M. B., Assumpção, M., Ruiz, M., Alvarado, P., Condori, C., & Lynner, C. (2020). Mantle dynamics of the Andean Subduction Zone from continent-scale teleseismic S-wave tomography. *Geophysical Journal International*, 224(3), 1553–1571. https://doi.org/10.1093/gji/ggaa536

Russo, R. M., VanDecar, J. C., Comte, D., Mocanu, V. I., Gallego, A., & Murdie, R. E. (2010). Subduction of the Chile Ridge: Upper mantle structure and flow. *GSA Today*, 20(9), 4–10. https://doi.org/10.1130/GSATG61A.1

Sanhueza, J., Yáñez, G., Buck, W. R., Araya Vargas, J., & Veloso, E. (2023). Ridge Subduction: Unraveling the Consequences Linked to a Slab Window Development Beneath South America at the Chile Triple Junction. *Geochemistry, Geophysics, Geosystems*, *24*(9), e2023GC010977. https://doi.org/10.1029/2023GC010977

Schepers, G., van Hinsbergen, D. J. J., Spakman, W., Kosters, M. E., Boschman, L. M., & McQuarrie, N. (2017). South-American plate advance and forced Andean trench retreat as drivers for transient flat subduction episodes. *Nature Communications*, 8(1), 15249. https://doi.org/10.1038/ncomms15249

Scire, A., Zandt, G., Beck, S., Long, M., & Wagner, L. (2017). The deforming Nazca slab in the mantle transition zone and lower mantle: Constraints from teleseismic tomography on the deeply subducted slab between 6°S and 32°S. *Geosphere*, 13(3), 665–680. https://doi.org/10.1130/GES01436.1

Scire, A., Zandt, G., Beck, S., Long, M., Wagner, L., Minaya, E., & Tavera, H. (2016). Imaging the transition from flat to normal subduction: Variations in the structure of the Nazca slab and upper mantle under southern Peru and northwestern Bolivia. *Geophysical Journal International*, 204(1), 457–479. https://doi.org/10.1093/gji/ggv452

Siebert, L., Simkin, T., 2002. Volcanoes of the World: an Illustrated Catalog of Holocene Volcanoes and their Eruptions. Smithsonian Institution, Global Volcanism Program, Digital Information Series, GVP-3 Http://www.volcano.si.edu/world/.

Simmons, N. A., Myers, S. C., Johannesson, G., & Matzel, E. (2012). LLNL-G3Dv3: Global P wave tomography model for improved regional and teleseismic travel time prediction. *Journal of Geophysical Research: Solid Earth*, 117(B10). https://doi.org/10.1029/2012JB009525

Stern, C. R., & Kilian, R. (1996). Role of the subducted slab, mantle wedge and continental crust in the generation of adakites from the Andean Austral Volcanic Zone. *Contributions to Mineralogy and Petrology*, 123(3), 263–281. https://doi.org/10.1007/s004100050155

Suárez, G., Molnar, P., & Burchfiel, B. C. (1983). Seismicity, fault plane solutions, depth of faulting, and active tectonics of the Andes of Peru, Ecuador, and southern Colombia. *Journal of Geophysical Research: Solid Earth*, 88(B12), 10403–10428. https://doi.org/10.1029/JB088iB12p10403

Thorkelson, D. J. (1996). Subduction of diverging plates and the principles of slab window formation. *Tectonophysics*, 255, 47–63. https://doi.org/10.1016/0040-1951(95)00106-9

Thorkelson, D. J., & Breitsprecher, K. (2005). Partial melting of slab window margins: Genesis of adakitic and non-adakitic magmas. *Lithos*, 79(1–2), 25–41. https://doi.org/10.1016/j.lithos.2004.04.049

Thorkelson, D. J., & Taylor, R. P. (1989). Cordilleran slab windows. *Geology*, 17(9), 833–836. https://doi.org/10.1130/0091-7613(1989)017<0833:CSW>2.3.CO;2

Veloso, E. A. E., Anma, R., & Yamazaki, T. (2005). Tectonic rotations during the Chile Ridge collision and obduction of the Taitao ophiolite (southern Chile). *Island Arc*, 14(4), 599–615. https://doi.org/10.1111/j.1440-1738.2005.00487.x